

Towards Smart Blades for Vertical Axis Wind Turbines: Different Airfoil Shapes and Tip Speed Ratios

M. Rasoul Tirandaz¹, Abdolrahim Rezaeiha^{2,3}, Daniel Micallef¹

¹University of Malta, Department of Environmental Design, Msida, MSD2080, Malta

²KU Leuven, Leuven, Belgium

³Eindhoven University of Technology, Eindhoven, The Netherlands

Correspondence to: M. Rasoul Tirandaz (msctirandaz@gmail.com)

Abstract. Future wind turbines will benefit from state-of-the-art technologies that allow them to not only operate efficiently in any environmental condition, but also to maximize the power output and cut the cost of energy production. Smart technology, based on morphing blades, is one of the promising tools that could make this possible. The present study serves as a first basis-step towards for identifying designing morphing ing airfoils blades as functions of azimuthal angle and tip speed ratio for vertical axis wind turbines. The focus of this work is on the individual/combined quasi-static analysis of three airfoil shape-defining parameters, namely the maximum thickness t/c and its chordwise position xt/c as well as the leading-edge radius index I . A total of 126 airfoils are generated for a single-blade H-type darrieus turbine with a fixed blade/spoke connection point at $c/2$. The analysis is based on 630 high-fidelity transient 2D CFD simulations, previously validated with three experiments. The results show that with increasing tip speed ratio, the optimal maximum thickness decreases from 24% c to 10% c , its chordwise position shifts from 35% c to 22.5% c , while the corresponding leading-edge radius index remains at 4.5. The results show an average relative improvement of 0.46, and an average improvement-increase of nearly 0.06 in C_p for all the values of tip speed ratio.

Keywords. Smart rotor design; Morphing airfoil; Shape adaptation; Computational fluid dynamics (CFD); Floating offshore wind turbine (FOWT) Wind energy; Computational fluid dynamics (CFD).

Nomenclature

α	Angle of attack [°]	k	Reduced frequency, $\Omega c/2V_{ref} \approx c/2R$ [-]
α_{ss}	Static stall angle [°]	L	Lift [N]
θ	Azimuth angle [°]	M	Turbine moment [Nm]
λ	Tip speed ratio, $R\Omega/U_\infty$ [-]	n	Number of blades [-]
ν	Kinematic viscosity of air [m ² /s]	P	Turbine output power [W]
σ	Solidity, nc/d [-]	q	Dynamic pressure [Pa]
Ω	Turbine rotational speed [rad/s]	R	Turbine radius [m]
A	Turbine swept area, $h \cdot d$ [m ²]	Re_c	Chord-based Reynolds number, $cU_\infty\sqrt{1+\lambda^2}/\nu$ [-]
c	Airfoil chord length [m]	r_{LE}	Airfoil leading-edge radius [% c]
C_d	Drag coefficient, D/qA [-]	T	Turbine thrust force [N]
C_f	Skin friction coefficient, D/qA [-]	t/c	Airfoil relative maximum thickness [%]
C_l	Lift coefficient, L/qA [-]	U_∞	Freestream velocity [m/s]
C_m	Moment coefficient, $M/(qAR)$ [-]	U	Instantaneous streamwise velocity [m/s]
C_p	Turbine power coefficient, $P/(qAU_\infty)$ [-]	V	Instantaneous lateral velocity [m/s]
C_T	Turbine thrust coefficient, $T/(qA)$ [-]	$V_{tan,n}$	Dimensionless instantaneous tangential velocity, $(ucos(\theta)+vsin(\theta))/U_\infty$ [-]
D	Drag [N]	V_{rel}	Relative velocity [m/s]
h	Turbine height [m]	xt/c	Dimensionless chordwise-position of airfoil maximum thickness [%]
I	Airfoil leading-edge radius index [-]	TI	Turbulence intensity [%]

1. Introduction

1.1 State of the art

Formatted: Font color: Auto

Formatted: Font color: Auto

Formatted: Font color: Auto

Formatted: Font color: Auto

Formatted: Font color: Auto

Formatted: Font: Italic, Font color: Auto, Complex Script
Font: Italic

Formatted: Font color: Auto

Formatted: Font color: Auto

Formatted: Font color: Auto

Formatted: Font color: Auto

Formatted: Font color: Auto

Formatted: Font color: Auto

Formatted: Font: Not Italic, Font color: Auto, Complex
Script Font: Not Italic

Formatted: Font color: Auto

Formatted: Font: 10 pt, Font color: Auto, Complex
Script Font: 10 pt

102 optimal airfoils at each λ , as well as each azimuth angle, and thus, making a conceptual step towards designing morphing blades
 103 for VAWTs.

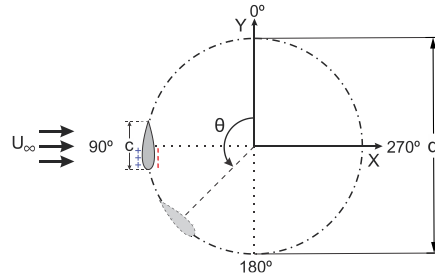
104 **1.3 Paper outline**

105 The paper is organized as follows: Sect. 2 presents the computational settings and parameters for the simulations. The solution
 106 verification and validation studies are also included. Sect. 3 introduces the generated airfoil shapes. In Sect. 4, the results are
 107 presented in two scenarios. Sect. 5, ~~and 6,~~ and 7 are devoted to the discussion, research limitations, and conclusions, respectively.

108 **2. Computational settings and parameters**

109 **2.1 Reference turbine characteristics**

110 A single-bladed Darrieus H-type VAWT was chosen as the reference case for this study (see Fig. 1 and Table 1). The turbine is a
 111 simplified representation of the original one used by (Tescione et al., 2014). That is, the turbine shaft and spokes are removed, and
 112 there is only one blade. Note that the conclusions are not significantly affected by these components. The reader is referred to our
 113 earlier works (Rezaeiha et al., 2017b; Rezaeiha et al., 2018a) where it is shown that for low solidity VAWTs, the power
 114 performance is almost independent of the shaft and number of blades. Therefore, such a simplified turbine model can effectively
 115 reduce the computational costs of the huge number of simulations (i.e., 630 transient simulations) for the present work and, at the
 116 same time, provide reliable results. Refs. (Rezaeiha et al., 2018a, b) are used to select the rest of the geometrical and operational
 117 characteristics of the reference turbine.



118
 119 **Figure 1: The reference turbine (not to scale). (+): airfoil pressure side and (-): suction side for $0^\circ \leq \theta < 180^\circ$.**

120 **Table 1: Characteristics of the reference turbine.**

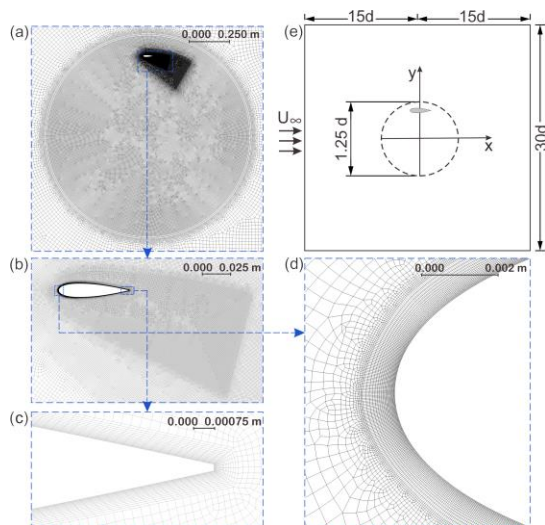
Turbine type	Darrieus H-type
n	1
d	1 m
σ	0.06
Airfoil shape	NACA0018-6.0/3.0 (i.e., baseline NACA0018) $t/c = 18\%$; $l = 6.0$; $xt/c = 30\%$
Blade/Spoke connection point	$c/2$
U_∞	9.3 m/s
λ	2.5, 3.0, 3.5, 4.5, 5.0
Ω	46.5, 55.8, 65.1, 83.7, 93.0 rad/s
c	0.06 m
$Re_c [\times 10^5]$	1.03, 1.20, 1.40, 1.76, 1.95
TI	5%

121 **2.2 Computational settings**

122 The commercial flow solver ANSYS Fluent v2019R2 is employed for the 2D incompressible URANS simulations coupled with
 123 the four-equation transition SST turbulence model. The simulations are solved using second-order spatial/temporal discretization
 124 and the SIMPLE pressure-velocity coupling scheme. The computational domain, grid, and boundary conditions are summarized
 125 in Table 2. The schematic of the computational domain and the computational grid and its subregions are shown in Fig.2.

126 Some attempts have been made to identify the proper computational settings for the simulation of H-type Darrieus turbine
 127 (Balduzzi et al., 2016a; Balduzzi et al., 2016b). However, in this work, the turbulence model is selected based on our previous
 128 findings (Rezaeiha et al., 2019b, 2020a). Best-practice guidelines for the CFD simulations of VAWTs are used to select the domain
 129 size, the azimuthal increment, and the convergence criterion (Rezaeiha et al., 2018c). The corresponding absolute time-step values
 130 are $3.75339546 \times 10^{-5}$ s, $3.12782955 \times 10^{-5}$ s, $2.68099676 \times 10^{-5}$ s, 2.0852197×10^{-5} s and $1.70608885 \times 10^{-5}$ s for $\lambda = 2.5, 3.0, 3.5, 4.5$
 131 and 5.5, respectively. With the selected $d\theta = 0.1$, 3600 time-steps per turbine revolution are achieved. A total number of 20
 132 revolutions, i.e., 72,000 time-steps, are simulated before the results of the present study are obtained at the 21st turbine revolution.
 133 Under these conditions, the statistical convergence of the transient simulations is ensured. In each case, a number of 20 iterations
 134 per time-step is performed so that the scaled residuals stay $< 10^{-5}$.

Formatted: Font color: Auto
 Formatted: Font: 10 pt, Complex Script Font: +Headings CS (Times New Roman), 10 pt



135
 136 **Figure 2. (a-d) the grid; and (e) schematic of the computational domain (not to scale).**

137 **Table 2: Details of computational domain, grid, and boundary conditions.**

Computational domain (see Fig. 2e)	$30d \times 30d$ (d : turbine diameter)
Computational grid (see Fig. 2a-d)	Cell type: quadrilateral Cell No.: 302,815 No. of cells around the airfoil circumference: 800
Boundary conditions	$y_{max}^+ < 2.5$ Inlet: uniform normal velocity (Turbulence length scale = d); Outlet: zero static gauge pressure;

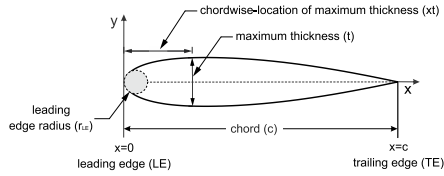
138 **2.3 Solution verification and validation**

139 The domain type is selected based on our earlier studies, where the difference between 2D and 2.5D URANS simulations was
140 found to be insignificant-(Rezaeiha et al., 2018b)(Rezaeiha et al., 2017a). A grid convergence analysis using uniformly-doubled
141 grids has been performed and documented in Ref. (Rezaeiha et al., 2019c), which for brevity is not repeated here. Three
142 experimental studies with different test conditions ~~previously are-were~~ used to validate the CFD simulations. The different
143 geometrical and operational characteristics of the turbines used in the experiments led to dissimilar conclusions (Tescione et al.,
144 2014; Ferreira et al., 2009; Castelli et al., 2011), ensuring a high level of confidence in the accuracy of the CFD simulations.
145 However, the reader is referred to Ref. (Rezaeiha et al., 2019b) for more detailed descriptions of the validation studies.

146 **3. Morphing airfoil shape modifications**

147 Figure 3 shows a schematic drawing of the symmetric modified NACA 4-digit airfoil and the selected shape-defining parameters
148 for this study. These parameters are ~~morphed-modified~~ within their most common regimes as follows:

- 149 (i) relative maximum thickness (t/c): 10, 12, 15, 18, 21 and 24%;
- 150 (ii) relative chordwise position of maximum thickness (xt/c): 20, 22.4, 25, 27.5, 30, 35 and 40%;
- 151 (iii) index of leading-edge radius (J): 4.5, 6.0 and 7.5.



152 **Figure 3: Defining parameters of the symmetric airfoil.**

Formatted: Indent: First line: 0"

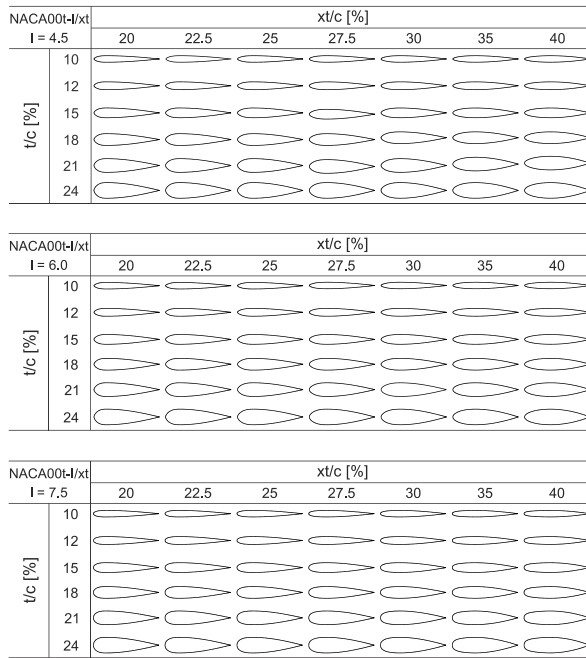


Figure 4: Studied airfoil shapes.

Note that any value of I out of the selected range results in a too sharp or too blunt leading edge. The analysis is based on 126 airfoil shapes (see Fig. 4). The modification of the airfoil coordinates and the related equations are documented in Ref. (Tirandaz and Rezaeiha, 2021). The focus of this study is on symmetric airfoils with zero camber. The morphing-modified airfoils are designated as the $NACA00I-t/c - I / xt/c$. The first symbol from left to right, i.e., t/c , represents the maximum thickness in %c; the second one, I , shows the index of leading-edge radius (with one decimal precision); and the third one, xt/c , is the chordwise position of the maximum thickness in 10^{th} of the chord with two decimal precision. For example, the NACA0024-4.5/35.0 has a maximum thickness of $t/c = 24\%$, located at $xt/c = 35\%$, and a leading-edge radius index of $I = 4.5$.

4. Results

The results are presented in two scenarios, namely, morphing-optimal airfoils as functions of λ (Sect. 4.1), and $d\theta$ (Sect. 4.2). In Sect. 4.3 the performance of the morphing-optimal airfoils from the first scenario are compared with that of the reference airfoil. A coupled analysis is performed at different λ of 2.5, 3.0, 3.5, 4.5 and 5.5. Figure 5 depicts the variations of α as the turbine passes through its last revolution. Note that the higher the value of λ is, the more limited the variations of α is are. For $\lambda = 2.5, 3.0$ and 3.5 , the variations of α exceeds the α_{st} for all the studied airfoils; while at higher $\lambda = 4.5$ and 5.5 , this behaviour is not observed for all of the studied airfoils~~not for all the studied airfoils the same event is observed~~. The reader is referred to (Rezaeiha et al., 2018b), where the method of calculating the α from the CFD results is provided in detail. However, in a recent study by (Melani et al., 2020) an ad hoc inverse verification procedure was developed to compare the accuracy of three selected methods in calculating the angle of attack from the CFD flow field, including 3-Points, Line Average, and Trajectory approaches.(Melani et al., 2020a)

- Formatted: Space After: 0 pt
- Formatted: Font: Italic, Complex Script Font: Italic
- Formatted: Font: Italic, Complex Script Font: Italic
- Formatted: Font: (Default) +Headings CS (Times New Roman), 10 pt, Font color: Auto, Complex Script Font: +Headings CS (Times New Roman), 10 pt
- Formatted: Font: 10 pt, Complex Script Font: +Headings CS (Times New Roman), 10 pt
- Formatted: Font: 10 pt, Complex Script Font: +Headings CS (Times New Roman), 10 pt
- Formatted: Font: 10 pt, Complex Script Font: +Headings CS (Times New Roman), 10 pt

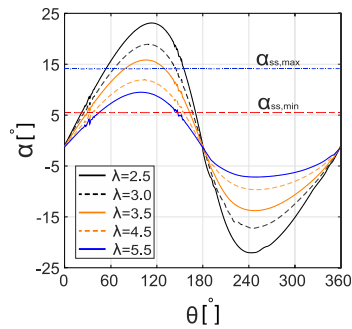


Figure 5: α versus θ for different λ . The $\alpha_{ss,min}$ and $\alpha_{ss,max}$ are based on Xfoil.

4.1 Morphing Modification of the airfoil shape-defining parameters

To derive the optimal airfoil for each λ , the combination of the t_{opt}/c , xt_{opt}/c , and I_{opt} , corresponding to the turbine $C_{P,max}$ is determined. Sect. 4.1.1 to 4.1.3 are devoted to the discussions on individual **morphing modification**, and Sect. 4.1.4, presents an overall view on the combined **morphing modification** of the aforementioned parameters.

4.1.1 Morphing Modification of the maximum thickness (t/c)

Figure 6 shows the impact of **morphing changing** t/c on the turbine C_P for the studied range of xt/c , I and λ . Figure 7 shows the instantaneous moment coefficient C_m versus θ for selected t/c and xt/c . It can be observed that:

Regarding the lowest value of $I = 4.5$ (see Fig. 6a – e and Fig. 7): Generally speaking, the trend of $C_P - t/c$ for different λ is similar, except for some noticeable differences. That is, by increasing λ , the C_P shows higher sensitivity to t/c . This is reflected as higher $|AC_P|$ and **can be explained by the following reasoning**: by **morphing changing** t/c , the pressure gradient changes over the airfoil; therefore, the transition point, the separation and stall characteristics, and eventually the resultant aerodynamic loads also change. However, when the flow is fully separated in the post-stall regime, **morphing changing** t/c has no longer significant impact on C_P . By increasing λ , and thus, more limited variation of α , the blade passes over a range of fewer azimuth angles in the post-stall regime (see Fig. 5). Due to this, **morphing changing** the t/c is influential within a wider range of effective θ . This can be recognized by the improved C_P for higher λ . At $\lambda = 2.5$, the C_P follows a **polynomial-non-monotonic** trend for $xt/c \leq 30\%$, and a monotonic upward trend for $xt/c \geq 35\%$. Nevertheless, with the exception of $xt/c \leq 22.5\%$ at $\lambda = 5.5$, where the C_P monotonically decreases by increasing t/c , the trend remains **polynomial-non-monotonic** for different values of xt/c at the studied range of λ . That is, by **changing the positive morphing of t/c to higher values**, the C_P experiences an initial growth to its maximum value at t_{opt}/c , followed by a reduction for $t/c > t_{opt}/c$. This can be recognized from the C_m plots, where by **morphing changing** t/c to its optimal value at t_{opt}/c , the sudden drop in $C_{m,max}$, which indicates the instant of moment stall, is observed at higher θ ; the consequent fluctuation is alleviated, and the **overall-mean** value of C_m increases, thus, making consistency with the highest C_P at t_{opt}/c for a fixed xt/c (see Fig. 7a-i for selected xt/c). This can be attributed to the following observations from the skin friction, lift, and drag coefficients (C_f , C_l , and C_d): when the turbine is operating at low values of $\lambda \leq 3.5$, increasing t/c from 10% to t_{opt}/c , changes the stall type from **leading-edge stall mixed stall and thin airfoil stall** for $t/c \leq 10\%$ to trailing-edge stall for **moderate and high-thickness** airfoils; **with $t/c \geq 15\%$** ; an earlier formation of laminar separation bubble (LSB) and trailing-edge separation (TES) is observed; TES-LSB merging (i.e., full-flow separation) is discovered to occur at higher azimuth, indicating a more extended favorable pressure gradient for t_{opt}/c (see for example Fig. 8 for $xt/c = 27.5\%$ at $\lambda = 2.5$); **the lighter**

Formatted: Indent: First line: 0"

Formatted: Font: (Default) +Headings CS (Times New Roman), 10 pt, Font color: Auto, Complex Script Font: +Headings CS (Times New Roman), 10 pt

Formatted: Font: Italic, Complex Script Font: Italic

Formatted: Font: Italic, Font color: Auto, Complex Script Font: Italic

dynamic stall characteristics is observed; that is, (i. e., jump in lift and drag coefficients, and post-stall load fluctuation) are significantly reduced; and the deviation in lift and drag, lift and drag jump, which indicates the onset of dynamic stall, reduce and shifts to higher azimuth, and the consequent post-stall loads fluctuations are alleviated (see for example Fig. 9 for $xt/c = 27.5\%$ at $\lambda = 2.5$). However, an earlier stall is found to occur for $t/c > t_{opt}/c$ due to more pronounced earlier merging of TES-LSB. This is reflected by lower C_p and $C_{m,max}$ for $t/c > t_{opt}/c$ (see Figs. 6a-c and 7a-i). Note that the monotonic growth in $C_p - t/c$ for $xt/c \geq 35\%$ at $\lambda = 2.5$ can also be explained with the aforementioned reasoning, yielding the $C_{p,max}$ at the highest thickness of $t_{opt}/c = 24\%$ (see Fig. 6a). For brevity, the skin friction, lift, and drag coefficients are not presented here.

Formatted: Font: (Default) +Headings CS (Times New Roman), 10 pt, Font color: Auto, Complex Script Font: +Headings CS (Times New Roman), 10 pt

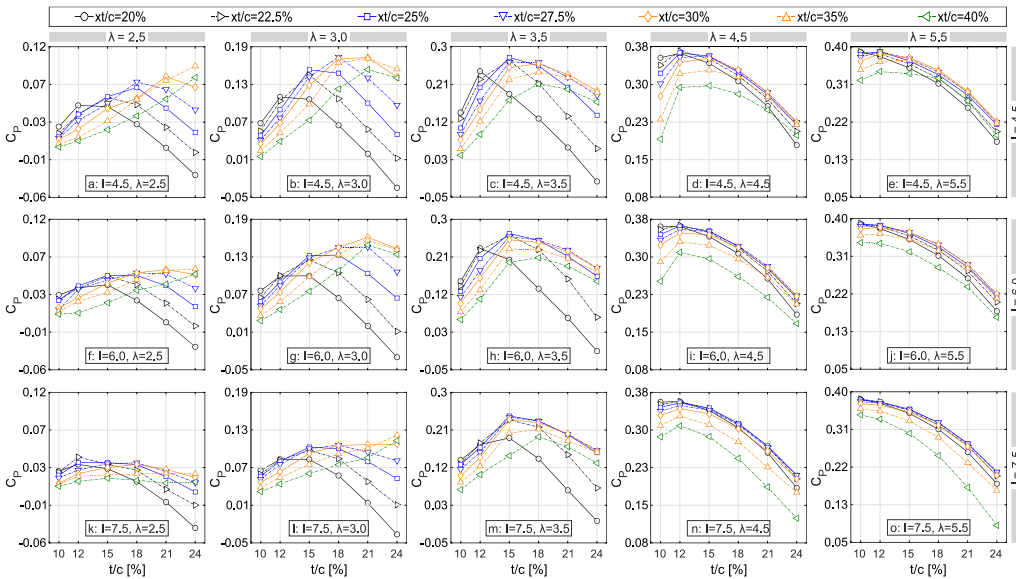


Figure 6: Impact of morphing changing t/c on the turbine C_p at different xt/c and λ .

Table 3 shows the t_{opt}/c , corresponding to each xt/c (i. e., $t_{opt,xt}/c$) at different λ . The t_{opt}/c corresponding to each λ is indicated by a star sign. It can be seen that by increasing xt/c , which means a longer favorable pressure gradient on the blade, a higher thickness is needed for the airfoil to be optimal. Note that, increasing λ , influences the shape of the optimal airfoil by decreasing its thickness. In other words, the higher λ is, the thinner the optimal airfoil is. This is consistent with the findings documented in (Healy, 1978; Subramanian et al., 2017), where it shows the superior performance of thick airfoils at low λ . This may be attributed to the turbine operational regime as follows: When the turbine goes into regimes with higher λ and more pronounced reduction in the variation of α , higher values of C_l at lower α is of most impact on the turbine C_p . Therefore, thinner airfoils with a higher lift curve slope outperform the thicker ones with a lower slope of the $C_l - \alpha$. Eventually, this results in less pronounced sensitivity of the t_{opt}/c to xt/c , and shifting the peak in $C_p - t/c$ (i. e., t_{opt}/c) towards the lowest $t/c = 10\%$ and 12% in the non-dynamic stall regime with $\lambda \geq 4.5$ (see Table 3). The analysis also shows a drag increment for thicker airfoils at $\lambda = 4.5$ and 5.5 , which is a result of the earlier formation of LSB and TES. This is consistent with the reduction in C_p and $C_{m,max}$ for $t/c > t_{opt}/c$ (see Figs. 6d-e and 7j-o). Note that for $xt/c \leq 22.5\%$ at $\lambda = 5.5$ the same reasoning results in a monotonic decrease of C_p , yielding the $C_{p,max}$ at the lowest thickness of $t/c = 10\%$.

The effect of flow curvature on aerodynamic loading is another important physical phenomenon to take into account in predicting the performance of VAWTs. Because of the angular velocity of the turbine rotor blades, the relative flow direction continuously varies along the airfoil chord, and thus, the blades experience curved streamlines. As a result of this, a symmetrical airfoil with zero pitch angle in the circular path of a VAWT rotor behaves as if it's a cambered airfoil with a non-zero pitch angle in a straight flow (Migliore et al., 1980) (Migliore et al., 1980; Rainbird et al., 2015). The flow curvature effects become less pronounced on a curved airfoil (Coiro et al., 2005). In addition, a blade hinge located at 50% chord length significantly alleviates the flow curvature effects (Coiro et al., 2005). However, among all the parameters, the ratio of blade chord to turbine rotor radius (c/R) has the greatest impact on flow curvature effects (Migliore et al., 1980). For low values of c/R (i.e., low solidity), the blade surface pressure distribution shows negligible differences with respect to that of the no-lift condition (Coiro et al., 2005), indicating less pronounced effects of flow curvature on the performance of low-solidity turbines (Coiro et al., 2005; Rainbird et al., 2015) (Rainbird et al., 2015). In this study, due to the low value of $c/R = 0.12$ (i.e., low σ), the contribution of flow curvature effects is considered to be small.

Regarding the moderate and highest values of $I = 6.0$ and 7.5 (see Fig. 6f-j and 6k-o): The overall trend for C_p is very similar to that of the lowest $I = 4.5$; however, it shows comparatively lower values of $|\Delta C_p|$, especially for $\lambda \leq 3.5$. The impact of morphing changing the r_{LE} on the turbine C_p is separately discussed in detail in Sect. 4.1.3; therefore, it is not included here.

Table 3: $t_{opt,x}/c$ for different values of xt/c and λ ($I = 4.5$).

λ	20	22.5	25	27.5	30	35	40	xt/c [%]
2.5	12	15	18	18	21	24*	24	$t_{opt,x}/c$ [%]
3.0	12	15	15	18*	21	21	21	
3.5	12	15	15*	15	18	18	18	
4.5	12	12*	12	15	15	15	15	
5.5	10	10*	12	12	12	15	12	
* t_{opt}/c at the corresponding λ								

Formatted: Font: 10 pt, Complex Script Font: +Headings CS (Times New Roman), 10 pt

Formatted: Font: 10 pt, Complex Script Font: +Headings CS (Times New Roman), 10 pt

Formatted: Font: 10 pt, Complex Script Font: +Headings CS (Times New Roman), 10 pt

Formatted: Font: 10 pt, Complex Script Font: +Headings CS (Times New Roman), 10 pt

Formatted: Font: 10 pt, Complex Script Font: +Headings CS (Times New Roman), 10 pt

Formatted: Font: 10 pt, Complex Script Font: +Headings CS (Times New Roman), 10 pt

Formatted: Font: 10 pt, Complex Script Font: +Headings CS (Times New Roman), 10 pt

Formatted: Font: 10 pt, Complex Script Font: +Headings CS (Times New Roman), 10 pt

Formatted: Font: 10 pt, Font color: Auto, Complex Script Font: 10 pt

Formatted: Font: 10 pt, Complex Script Font: +Headings CS (Times New Roman), 10 pt

Formatted: Font: Italic, Font color: Auto, Complex Script Font: Italic

Formatted: Font: 10 pt, Complex Script Font: +Headings CS (Times New Roman), 10 pt

Formatted: Font: 10 pt, Complex Script Font: +Headings CS (Times New Roman), 10 pt

Formatted: Font: 10 pt, Complex Script Font: +Headings CS (Times New Roman), 10 pt

Formatted: Font: Italic, Font color: Auto, Complex Script Font: Italic

Formatted: Font: 10 pt, Complex Script Font: +Headings CS (Times New Roman), 10 pt

Formatted: Font: 10 pt, Complex Script Font: +Headings CS (Times New Roman), 10 pt

Formatted: Font: 10 pt, Complex Script Font: +Headings CS (Times New Roman), 10 pt

Formatted

Formatted

Formatted

Formatted

Formatted

Formatted

Formatted

Formatted

Formatted: Font: Italic, Complex Script Font: Italic

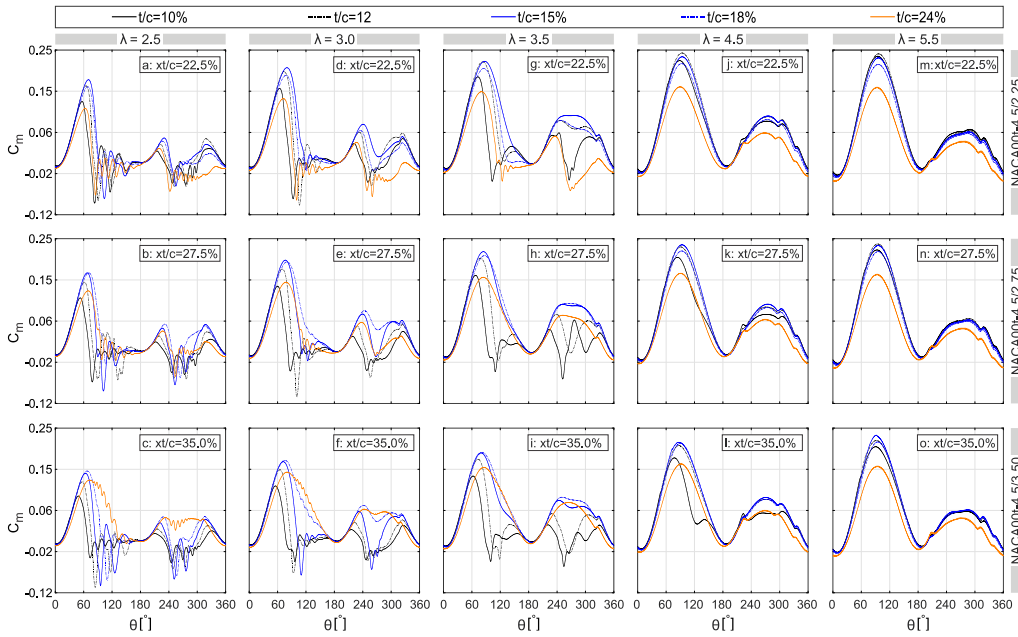


Figure 7: Impact of **changemorphing** t/c on the turbine C_m for selected xt/c and t/c at different λ .

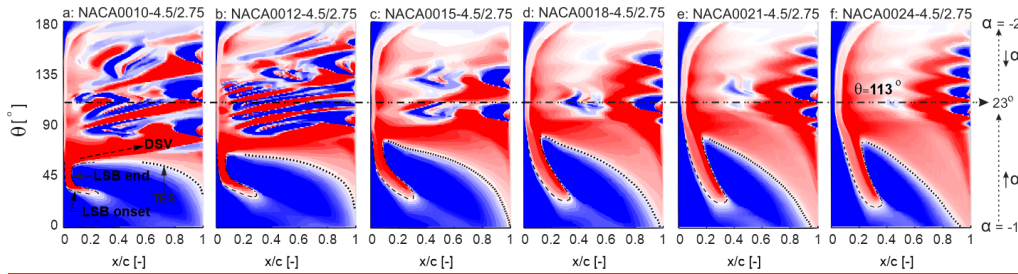
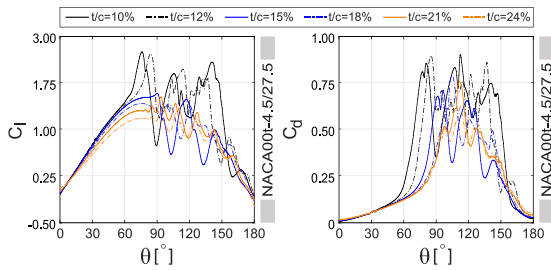


Figure 8: Spatiotemporal contour plots of C_r along the suction side of the blade during the first-half of the last revolution for the NACA001-4.5/27.5 at $\lambda = 2.5$. Note that the X-axis is along the chord line and $\theta = 113^\circ$ corresponds to the blade's $\rho_{max} = 23^\circ$.



- Formatted: Indent: First line: 0"
- Formatted: Font color: Auto
- Formatted: Font color: Auto
- Formatted: Font color: Auto
- Formatted: Font color: Auto
- Formatted: Font: 9 pt, Italic, Complex Script Font: 9 pt, Italic
- Formatted: Font: 9 pt, Complex Script Font: 9 pt
- Formatted: Font: 9 pt, Not Italic, Complex Script Font: 9 pt, Not Italic
- Formatted: Font: 9 pt, Complex Script Font: 9 pt
- Formatted: Font: 9 pt, Not Italic, Complex Script Font: 9 pt, Not Italic
- Formatted: Font color: Auto
- Formatted: Font color: Auto
- Formatted: Font: 9 pt, Complex Script Font: 9 pt
- Formatted: Indent: First line: 0"

246 **Figure 9. Impact of t/c on variations of C_l and C_d versus β , during the first-half of the turbine last revolution for $xt/c = 27.5\%$, and $I = 4.5$**
247 **at $\lambda = 2.5$.**

248 4.1.2 Morphing-Modification of the chordwise position of maximum thickness (xt/c)

249 Figure 108 shows the variation of the turbine C_p versus xt/c at the studied range of t/c , I , and λ . Figure 119 shows the instantaneous
250 moment coefficient C_m versus azimuth for selected xt/c and t/c . It can be seen that:

251 *Regarding the lowest value of $I = 4.5$ (ee Fig. 108a-e):* The overall trend of $C_p - xt/c$ for different λ is very similar, except for the
252 following differences. By increasing λ , the turbine C_p shows higher $|\Delta C_p|$. This is due to the similar reasoning discussed earlier in
253 Sect. 4.1.1, and summarized as follows: **morphing-changing the xt/c results in changing the boundary layer and stall characteristics.**

254 On the other hand, increasing λ is associated with lower variation of α , i.e., a more limited azimuthal range of the post-stall regime.
255 As a result, the impact of **morphing-changing the xt/c becomes significant over a wider range of θ , resulting in improved C_p .**

256 For $t/c \leq 12\%$ in the dynamic stall regime with $\lambda \leq 3.5$, the C_p monotonically decreases by **morphing-increasing the xt/c , yielding**
257 **the $C_{p,max}$ with the lowest xt/c of 20%** (see Fig. 108a-c). However, apart from $t/c = 10\%$ at $\lambda = 4.5$, where C_p monotonically

258 decreases, the trend for thin airfoils changes to **polynomial-non-monotonic** at $\lambda \geq 4.5$ (see Fig. 108d-e). In other words, by **morphing**
259 **increasing the xt/c from 20% to 40%, the C_p grows to its maximum value at xt_{opt}/c , before decreasing for $xt/c > xt_{opt}/c$.** **On one**

260 **hand,** the monotonic behavior of C_p for thin airfoils at low λ can be explained based on the observations of the skin-friction
261 coefficient C_f as follows: The dynamic stall for $t/c \leq 12\%$ is preceded by either (i) gradual extension of the LSB towards the trailing

262 edge (thin-airfoil stall), or (ii) a sudden upstream propagation of the TES (leading-edge stall). **Morphing-Changing the xt/c to higher**
263 **values results in either an earlier downstream extension of the LSB, or an earlier formation and abrupt-upstream propagation of**

264 **the TES; and consequently, an advanced stall on the blade. This is evident from the C_m plots for $t/c = 12\%$ (see Fig. 119a-c), where**
265 **the abrupt drop in $C_{m,max}$ occurs at a lower θ , indicating an earlier moment stall due to increasing the xt/c . The overall lower values**

266 **of C_m for higher xt/c justify the monotonic reduction in C_p . This can also be recognized from the C_l and C_d plots, where by increasing**
267 **xt/c , the deviation in lift and drag coefficients occurs at lower azimuth, signaling an earlier dynamic stall onset.** For brevity, the C_f

268 **, C_l , and C_d plots are not presented here.**

Formatted: Font: 9 pt, Bold, Not Italic, Complex Script
Font: 9 pt, Bold, Not Italic

Formatted: Font: 9 pt, Bold, Not Italic, Complex Script
Font: 9 pt, Bold, Not Italic

Formatted: Font: 9 pt, Bold, Not Italic, Complex Script
Font: 9 pt, Bold, Not Italic

Formatted: Font: 9 pt, Complex Script
Font: 9 pt

Formatted: Font: (Default) +Headings CS (Times New Roman), Bold, Not Italic, Font color: Auto, Complex Script
Font: +Headings CS (Times New Roman), Bold

Formatted: Font: (Default) +Headings CS (Times New Roman), Bold, Not Italic, Font color: Auto, Complex Script
Font: +Headings CS (Times New Roman), Bold, Not Italic

Formatted: Font: (Default) +Headings CS (Times New Roman), Bold, Not Italic, Font color: Auto, Complex Script
Font: +Headings CS (Times New Roman), Bold

Formatted: Font: (Default) +Headings CS (Times New Roman), Bold, Not Italic, Font color: Auto, Complex Script
Font: +Headings CS (Times New Roman), Bold, Not Italic

Formatted: Font: (Default) +Headings CS (Times New Roman), Bold, Not Italic, Font color: Auto, Complex Script
Font: +Headings CS (Times New Roman), Bold

Formatted

Formatted

Formatted

Formatted

Formatted

Formatted

Formatted

Formatted

Formatted

Formatted

Formatted

Formatted

Formatted

Formatted

Formatted

Formatted: Font color: Auto

Formatted: Font color: Auto

Formatted: Font color: Auto

Formatted: Font color: Auto

Formatted: Font color: Auto

Formatted: Font color: Auto

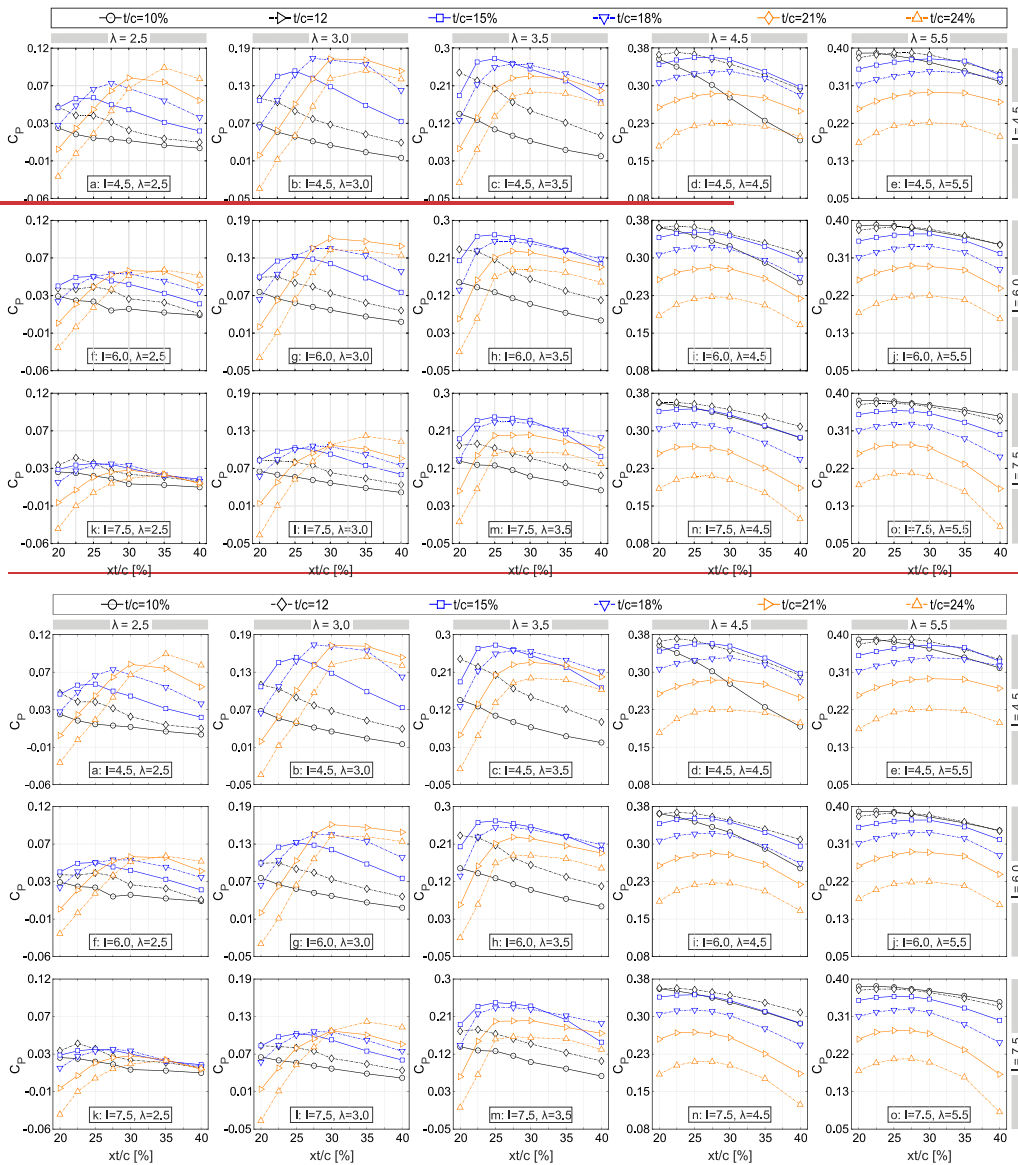


Figure 10: Impact of **morphing-changing** xt/c on the turbine C_p at different t/c and λ .

On the other hand, the **polynomial-non-monotonic** trend of C_p for thin airfoils at $\lambda \geq 4.5$ (i.e., non-dynamic stall regime) can be recognized from the C_m plots. For example, by **morphing-changing** the xt/c from 20% to $xt_{opt}/c = 25\%$ for $t/c = 12\%$ $\lambda = 5.5$, the $C_{m,max}$ slightly increases before decreasing for $xt/c \geq 27.5\%$ (see Fig. 108e). This can be explained by the skin-friction coefficient C_f , where it shows an earlier formation and upstream propagation of the TES, and thus, a **promoted TESn earlier stall** for $xt/c >$

Formatted: Font: Italic, Complex Script Font: Italic

Formatted: Font color: Auto

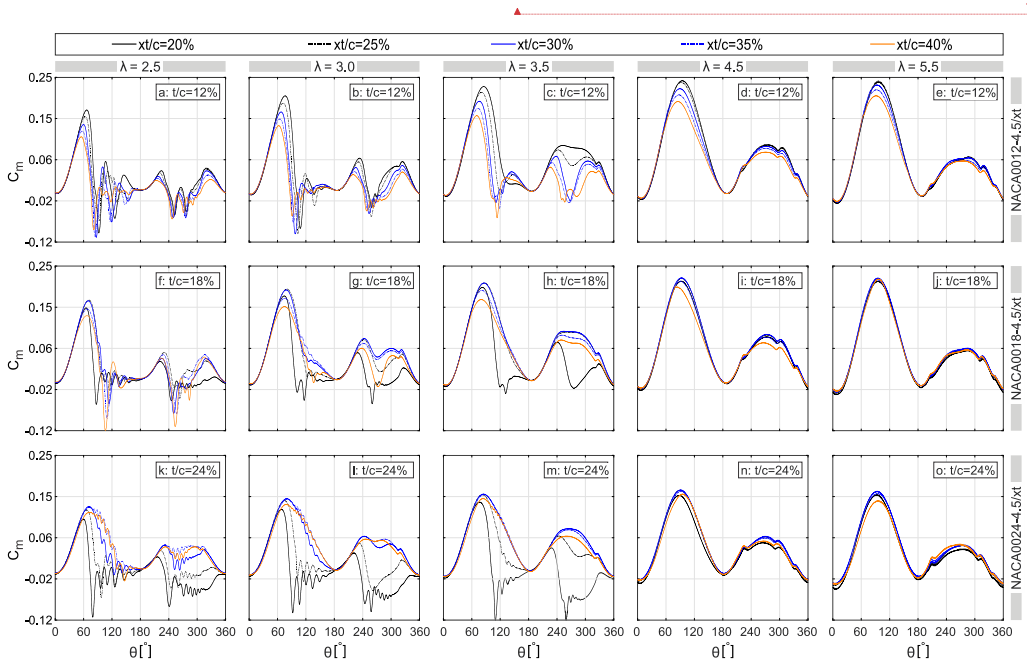
Formatted: Font color: Auto

xt_{opt}/c_x (see Fig. 12). Note that, when the adverse effects of dynamic stall are suppressed at $\lambda \geq 4.5$, increasing xt/c shows a marginal positive impact on the C_p for thin airfoils, reflecting a **polynomial-non-monotonic** trend of C_p versus xt/c . However, the value of t/c for thin airfoils plays a more crucial role in this regime. This can be observed from the sharp downward trend of $C_p - xt/c$ for $t/c = 10\%$ at $\lambda = 4.5$, while it changes to a **non-monotonic polynomial** trend for $t/c = 12\%$. This may be attributed to the more pronounced formation and propagation of TES, and thus, an earlier stall due to increasing xt/c for $t/c = 10\%$. However, the trend of $C_p - xt/c$ for t/c of 10% remains **non-monotonic polynomial** at $\lambda = 5.5$, showing less sensitivity to TES at higher λ . **For brevity, C_p contour plots are not presented here.**

Formatted: Font color: Auto

Formatted: Font color: Auto

Formatted: Font: Italic, Complex Script Font: Italic



Formatted: Font: 9 pt, Bold, Font color: Auto, Complex Script Font: 9 pt, Bold, Italic

Formatted: Centered, Space After: 10 pt, Line spacing: single, Keep with next, Border: Top: (No border), Bottom: (No border), Left: (No border), Right: (No border), Between: (No border)

Figure 11: Impact of **morphing changing** xt/c on the turbine C_m for selected t/c and xt/c at different λ .

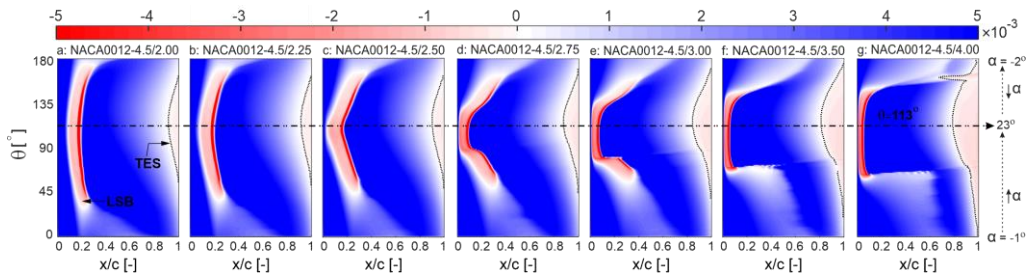


Figure 12: Spatiotemporal contour plots of C_f along the suction side of the turbine blade during the first-half of the last revolution for the NACA0012-4.5/ xt at $\lambda = 5.5$. Note that the X-axis is along the chord line and $\theta = 113^\circ$ corresponds to the blade's $\alpha_{max} = 23^\circ$.

For the medium- and high-thickness airfoils (i.e., $t/c \geq 15\%$), the turbine C_p polynomially follows a trend with a defined maxima increases at with xt_{opt}/c (see Figs. 108a-e). As previously discussed in Sect. 4.1.1, this polynomial-non-monotonic trend is a consequence of thicker-airfoil stall type, which is triggered by the formation of a flow reversal near the trailing edge (McCroskey, 1981; Sharma and Visbal, 2019; Frolov, 2016; Meseguer et al., 2007). Therefore, when xt/c morphs-changes to its optimal value, the adverse pressure gradient becomes less severe, resulting in improved stall characteristics. This can be recognized by either dynamic stall alleviation at low values of $\lambda \leq 3.5$, or a postponed stall at non-dynamic stall regimes with $\lambda \geq 4.5$. Table 4 gives the $xt_{opt,s}/c$ (i.e., the xt_{opt}/c at each t/c) in terms of $C_{p,max}$ for each λ . The corresponding xt_{opt}/c for different λ is indicated by a star sign. For $\lambda \leq 3.5$, by increasing t/c , the $xt_{opt,s}/c$ also increases. However, by increasing λ from 2.5 to 3.5, and thus, encountering a comparatively lighter dynamic stall and more limited variation of α , the xt_{opt}/c and its corresponding t/c decrease (see also Fig. 108). The reason for the outperformance of thin airfoils at higher λ is explained earlier in Sect. 4.1.1. Nevertheless, in the dynamic stall regime, the outperformance of moderate to high values of xt/c for thicker airfoils at a fixed λ is readily apparent from the turbine C_m for selected $t/c = 18\%$ and 24% (see Fig. 119f-h and k-m). It can be seen that increasing xt/c to its optimal value results in an increase in the C_m curve peak, a delay in the sudden drop of $C_{m,max}$, less pronounced subsequent fluctuations, and higher values of C_m in the turbine downwind quartile. This is due to alleviated dynamic stall, and is more pronounced for $t/c = 24\%$ (see Fig. 119k-m). A further increase in $xt/c > xt_{opt}/c$, is found to have a negative effect on C_m and finally leads to an earlier stall. This is because increasing the xt/c higher than xt_{opt}/c promotes the formation of LSB and TES, and results in an earlier full-flow separation and drop in $C_{L,max}$. Please note that for better illustration, the C_m plots are not presented for all the studied values of xt/c . For $\lambda \geq 4.5$, by morphing-increasing xt/c for $t/c \geq 15\%$, the C_p shows less sensitivity to xt/c and the corresponding xt_{opt}/c changes marginally (see Fig. 108d-e and Table 44). This is consistent with the turbine C_m plots for selected $t/c = 18\%$ and 24% , where the $C_{m,max}$ and the azimuth of moment stall are almost invariant to xt/c (see Fig. 119i-j and Fig. 119n-o).

Regarding the moderate and highest values of $I = 6.0$ and 7.5 (see Fig. 108f-j and 108k-o): The $C_p - xt/c$ shows a similar trend to that of $I = 4.5$. However, in dynamic stall regime (i.e., $\lambda \leq 3.5$), the turbine C_p shows a considerably smaller $|\Delta C_p|$, especially for higher xt/c . On the other hand, in non-dynamic stall regime with $\lambda \geq 4.5$, a marginal reduction in $|\Delta C_p|$ is observed. However, the $C_p - xt/c$ shows more pronounced sensitivity to morphing-changing xt/c for the moderate and thick airfoils.

Table 4: $xt_{opt,s}/c$ for $I = 4.5$ at different t/c and λ .

λ	10	12	15	18	21	24	t/c [%]
2.5	20	20	25	27.5	30	35*	$xt_{opt,s}/c$ [%]
3.0	20	20	25	27.5*	30	35	
3.5	20	20	25*	27.5	30	30	
4.5	20	22.5*	27.5	30	27.5	27.5	
5.5	22.5*	25	30	30	30	30	
* $xt_{opt,s}/c$ at the corresponding λ							

4.1.3 Modification of rphing the leading-edge radius (r_{LE})

Figure 130 shows the impact of morphing-changing r_{LE} on the C_p for selected and optimal airfoils at different λ . Figure 141 shows a comparison of the $C_p - xt/c$ for different I and selected values of t/c . The analysis is grouped based on the maximum thickness as follows:

Formatted: Font: 9 pt, Bold, Not Italic, Complex Script Font: 9 pt, Bold, Not Italic

Formatted: Font: 9 pt, Bold, Not Italic, Complex Script Font: 9 pt, Bold, Not Italic

Formatted: Font: Not Italic, Font color: Auto, Complex Script Font: Not Italic

Formatted: Font: Not Italic, Font color: Auto, Complex Script Font: Italic

Formatted: Font: Not Italic, Font color: Auto, Complex Script Font: Italic

Formatted: Font: 9 pt, Complex Script Font: 9 pt

Formatted: Font: 9 pt, Not Italic, Complex Script Font: 9 pt, Not Italic

Formatted: Font: Not Italic, Font color: Auto, Complex Script Font: Not Italic

Formatted: Font: Italic, Font color: Auto, Complex Script Font: Italic

Formatted: Font: (Default) + Headings CS (Times New Roman), 10 pt, Font color: Auto, Complex Script Font: + Headings CS (Times New Roman), 10 pt

Formatted: Font color: Auto

Formatted: Font color: Auto, Not Highlight

Formatted: Font color: Auto

Formatted: Font color: Auto

§19 Regarding the thin airfoils ($t/c = 10\%$ and 12%) (see Fig. 130 and 144a-e): regardless of xt/c , the turbine C_p is marginally
§20 influenced by the r_{LE} . This can be attributed to the low dependency of thin airfoils and the relevant aerodynamic loads on r_{LE} ,
§21 which is due to the geometrical constraints imposed by the airfoil thickness. It can be observed that by increasing the index of r_{LE}
§22 for different xt/c at $\lambda \leq 3.5$, C_p slightly changes; this minimal difference is in line with the corresponding C_m plots for $t/c \leq 12\%$.
§23 This can also be recognized from the skin friction, lift, and drag coefficients by the negligible changes in the characteristics of
§24 boundary layer events, including LSB and TES, and consequently the onset of dynamic stall and $C_{d,max}$. Due to the large volume
§25 of the results, the C_m , C_l , C_d , and C_f plots are not presented here. For $\lambda \geq 4.5$, except for the NACA0010-I/3.5, where increasing r_{LE}
§26 has the most influence on C_p , the aerodynamic loads and the turbine C_m show even less sensitivity to r_{LE} . Note that this is the
§27 regime in which the dynamic stall is no longer encountered and thin airfoils outperform the rest of the airfoils. The impact of r_{LE}
§28 on the turbine C_p for the optimal thin airfoils at $\lambda \geq 4.5$ is shown in Fig. 130f. Figures 152d and e show the corresponding C_m plots.
§29 Regarding the moderately-thick airfoils ($t/c = 15\%$ and 18%) (see Fig. 130 and 144f-j): overall, the turbine C_p shows higher
§30 dependency and sensitivity to r_{LE} . The higher dependency is due to the less severe geometrical constraints imposed by the
§31 moderately thick airfoils. Thus, ~~morphing-changing~~ the r_{LE} noticeably modifies the airfoil shape and thereby influences the
§32 aerodynamic loads. The higher sensitivity is reflected by the noticeable monotonic reduction of C_p for most of the xt/c values. This
§33 significant decrease can be recognized from the C_m plots, where the curve peak drops by ~~morphing-increasing~~ the leading edge
§34 ~~radius index, to more blunt shapes (i. e., higher r_{LE})~~. This may be due to the promoted LSB and TES characteristics, which result
§35 in higher $C_{d,max}$ for larger r_{LE} . For $\lambda \leq 3.0$, the more prominent sensitivity is observed within the range of $22.5\% \leq xt/c \leq 35\%$;
§36 however, the C_p shows less sensitivity to r_{LE} for $\lambda = 3.5$, corresponding to a lighter dynamic stall regime (see Fig. 144f-h). Note
§37 that the moderately thick airfoils show superior performance over the thin and thick airfoils at $\lambda = 3.0$ and 3.5 (i. e., the NACA0018-
§38 4.5/2.75 and NACA0015-4.5/2.5, respectively). Figure 130f and Figs. 152b and c show the impact of ~~morphing-changing~~ r_{LE} on
§39 the turbine C_p and C_m for the optimal airfoils at $\lambda = 3.0$ and 3.5 . When the turbine goes into the non-dynamic stall regime with $\lambda \geq$
§40 4.5, the range of xt/c within which the index of leading-edge radius is the most influential, shifts downstream to $30\% \leq xt/c \leq 40\%$
§41 (see Fig. 144i and j).

Formatted: Font color: Auto

Formatted: Font color: Auto

Formatted: Font color: Auto

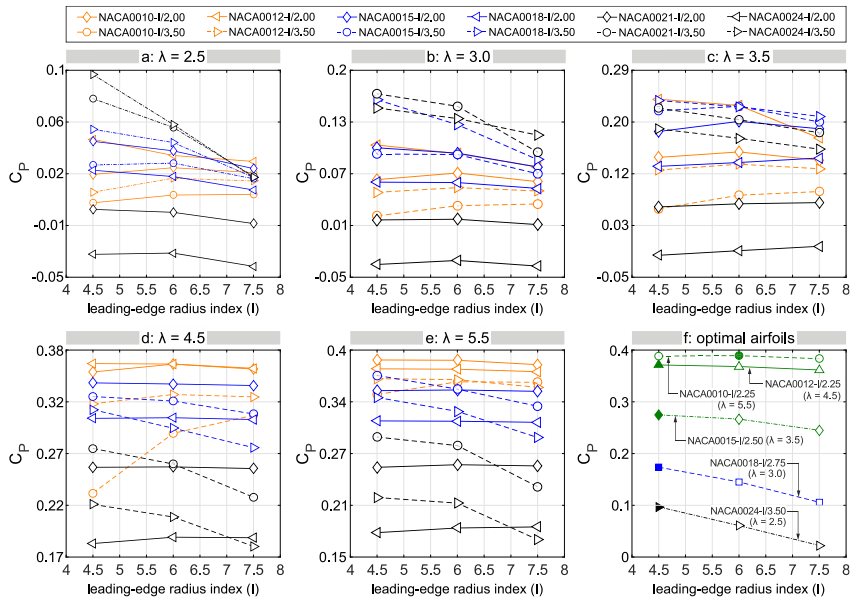


Figure 13: Impact of **morphing changing** r_{LE} on the C_P for (a-e) selected, and (f) optimal airfoils at different λ . Filled symbols represent the optimal airfoils corresponding to each λ .

Regarding the thick airfoils ($t/c = 21\%$ and 24%) (see Fig. 130 and 144k-o): the analysis shows that at $\lambda = 2.5$, thick airfoils significantly surpass other airfoils in terms of power performance (see Fig. 130). Aside from the following differences, the overall trend of $C_P - xt/c$ is quite similar to that of moderately thick airfoils: C_P values are more sensitive to r_{LE} at $\lambda = 2.5, 4.5$ and 5.5 , but less so at $\lambda = 3.0$ and 3.5 (see Fig. 144k-o). By increasing the r_{LE} , the C_P values experience a monotonic reduction, especially for thick airfoils with $xt/c \geq 30\%$ at $\lambda = 2.5$, where the variation of I is the most influential on C_P . For example, the overall reduction of C_P for the NACA0024-I/3.50 at $\lambda = 2.5, 3.0, 3.5, 4.5$ and 5.5 is 77%, 21%, 17%, 19% and 23%, respectively. This can be recognized from the C_m plots, where the C_m values decrease dramatically in both upwind and downwind quartiles, the C_m curve peak drops, and the post-stall C_m fluctuation gets more significant (see Fig. 152a). This is due to earlier formations of the LSB and TES, and thus a higher $C_{d,max}$. Thick airfoils with low xt/c show marginal sensitivity to r_{LE} at different λ . The corresponding C_m plots show approximately the same azimuth of moment stall for different I . For brevity, the C_m plots are only presented for the NACA0024-I/3.50, which is the optimal airfoil at $\lambda = 2.5$ (see Fig. 152a).

Overall, at $\lambda \leq 3.5$, the x_{top}/c belongs to the range of xt/c , which corresponds to the highest sensitivity of C_P to r_{LE} . For example, the optimal airfoil at $\lambda = 2.5$ (i.e., the NACA0024-4.5/3.5) has $xt/c = 35\%$ that fits in the range of $30\% \leq xt/c \leq 40\%$, within which the impact of r_{LE} is the most significant. This is while the x_{top}/c for $\lambda \geq 4.5$ (i.e., $xt/c = 22.5\%$) does not belong to such a range of xt/c (i.e., $xt/c \geq 30\%$). In addition, the most noticeable improvement in C_P due to **morphing changing** the r_{LE} occurs at $\lambda = 2.5$, where the dynamic stall deeply affects the aerodynamic and power performance of the blade. **Nevertheless**, by increasing λ and thus, alleviating or avoiding the dynamic stall, the aerodynamic loads are less affected by the r_{LE} .

Formatted: Font color: Auto

Formatted: Font: Italic, Font color: Auto, Complex Script
Font: Italic

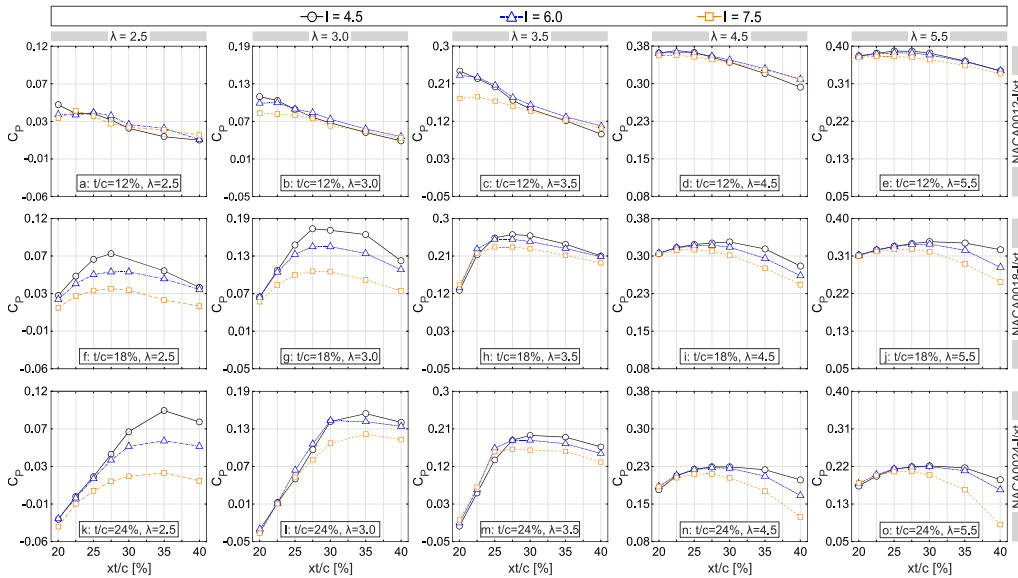


Figure 14: Comparison of the turbine C_p versus xt/c for different I and λ .

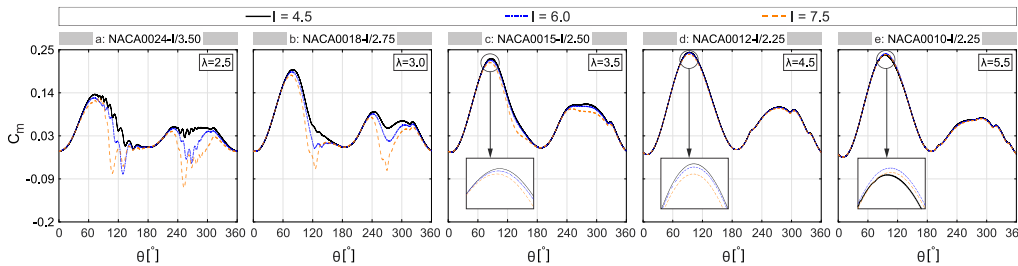


Figure 15: Impact of morphing-changing FLE on the turbine C_m for the combination of t_{opt}/c and xt_{opt}/c at different λ .

4.1.4 Combined morphing-modification of the airfoil shape-defining parameters

Morphing The airfoil shape-defining parameters have a coupled impact on turbine performance the airfoil shape-defining parameters is thought to have a fully coupled impact on the turbine C_P . Thus, it is of high importance to study the impact of their combined morphing-modification on the turbine C_P and C_T . Figure 163 shows the variation of C_P in $t/c - xt/c$ space for different I and λ . Except for $\lambda = 5.5$, where the combination of t_{opt}/c and xt_{opt}/c is achieved by the moderate $I = 6.0$, the $C_{p,max}$ corresponds to the smallest $I = 4.5$ for $\lambda \leq 4.5$.

For $\lambda = 2.5$ and $I = 4.5$, the global optimum occurs by a set of high t/c and xt/c (i.e., NACA0024-4.5/3.50). For higher $I = 6.0$, although the combination of t_{opt}/c and xt_{opt}/c -values remains invariant for $I = 6.0$; however, the region of maximum C_p shows lower values of $C_{p,-}$ the local optimum area is found to morph into thin airfoils with low xt/c . For $I = 7.5$, the morphing-optimal airfoil changes to a thin airfoil with low xt/c , while experiencing lower C_p compared to those of $I = 4.5$ and 6.0 . The variation of optimal airfoil shape-defining parameters for different λ and the resultant airfoils at each λ are illustrated in Fig. 174.

Formatted: Font color: Auto

Formatted: Font: (Default) + Headings CS (Times New Roman), 10 pt, Font color: Auto, Complex Script Font: + Headings CS (Times New Roman), 10 pt

Formatted: Font color: Auto

Formatted: Font color: Auto

Formatted: Font color: Auto

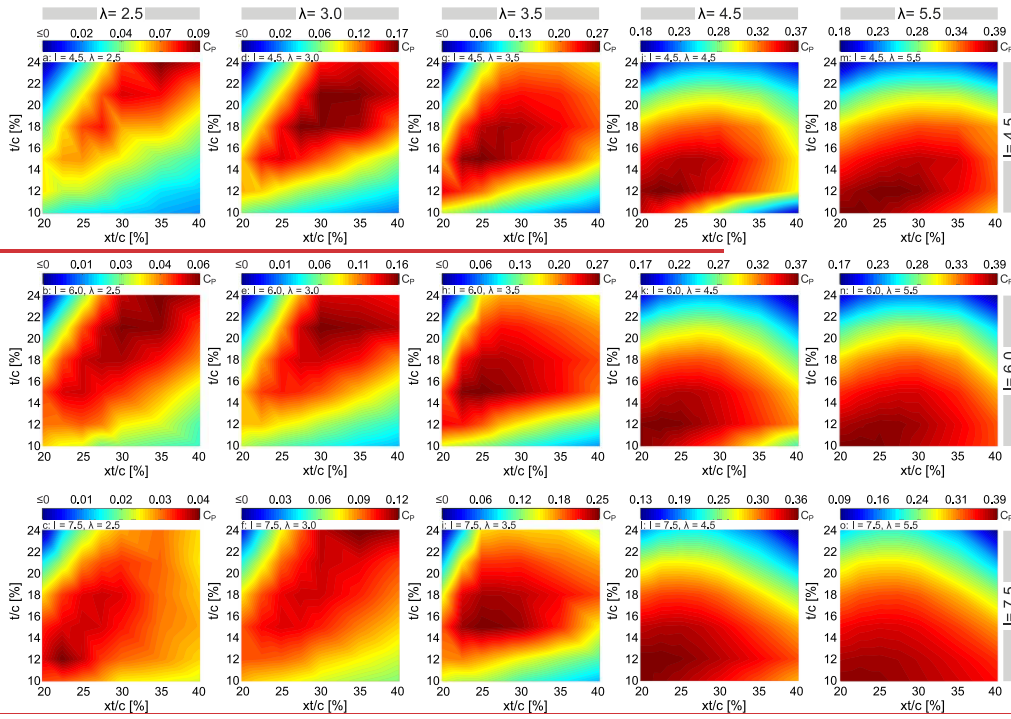
Formatted: Font color: Auto

Formatted: Font color: Auto

Formatted: Font color: Auto

378 At $\lambda = 3.0$, the region of $C_{p,max}$ shows less sensitivity to I , shifting between moderate and high values of t/c and xt/c (see Fig. 163d-
379 f). However, similar to that of $\lambda = 2.5$, the overall range of C_p values narrows down with increasing I . For $\lambda = 3.5$, the optimum
380 region of C_p remains nearly the same at moderate values of t/c and xt/c for different I (see Fig. 163g-i); while for higher values of
381 $\lambda \geq 4.5$, it stays approximately independent of I , shifting marginally between low values of t/c and xt/c (see Fig. 163j-o). This
382 implies that, by increasing λ , the optimum region of turbine C_p is less sensitive to I . ~~In other words, the higher λ is, the less~~
383 ~~dependent the local optimum is on I .~~ Overall, by increasing λ the local region of optimal airfoil shape-defining parameters changes
384 from the combination of high values of t/c and xt/c for $\lambda = 2.5$ to moderate t/c and xt/c for $\lambda = 3.0$ and 3.5, and low values of t/c
385 and xt/c for $\lambda \geq 4.5$.

Formatted: Font: Italic, Font color: Auto, Complex Script
Font: Italic



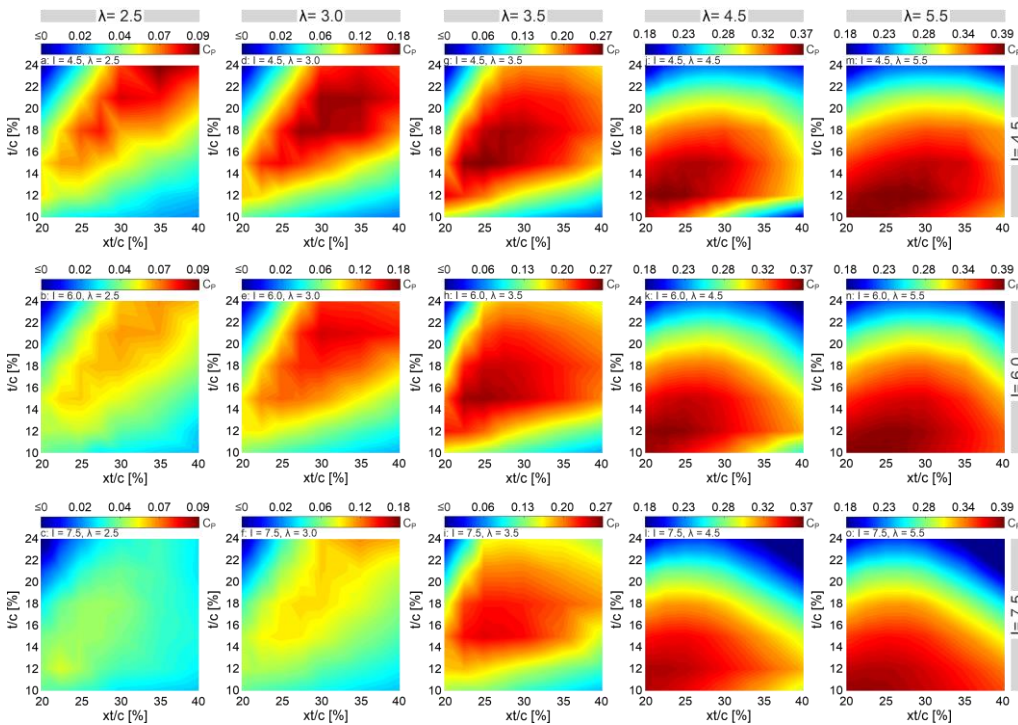


Figure 16: Turbine C_p in $t/c - xt/c$ space. Each contour plot is based on 42 simulations. Colormaps are in different range.

The results highlight that, it is observed that in designing morphing blades, single-parameter studies will not provide the overall picture and could lead to unreliable results. The contour plots give a conceptual view of the optimal regions in terms of the airfoil shape-defining parameters, with which the resultant airfoils have their most efficient performance; and also, the inefficient regions of the turbine C_p , which must be avoided.

Figure 185 shows the turbine C_T in $t/c - xt/c$ space. It is interesting to observe that for low $\lambda \leq 3.5$ there is no coincidence between the optimal regions of C_T and C_p contours; while for $\lambda \geq 4.5$, these two regions overlap. By increasing λ , the optimal region extends marginally towards higher t/c and xt/c , while also experiencing higher values of C_T . The noncongruent region of $C_{p,max}$ and $C_{T,max}$ at low values of λ is different from what is observed in the case of HAWTs. That is, the maximum power output of a HAWT occurs where the highest thrust load is exerted by the turbine blade on the flow. This led to a correlation between the regions of maximum optimal regions of C_p and C_T . In contrast, the results of the present study show that for VAWTs, the same phenomenon only occurs at high values of $\lambda \geq 4.5$, where the turbine goes into non-dynamic stall regimes with more limited variations of α . Therefore, when designing morphing blades for VAWTs, the C_T values corresponding to high values of λ are of more importance compared to those of lower λ , where dynamic stall is expected to occur.

Formatted: Font: (Default) +Headings CS (Times New Roman), 10 pt, Font color: Auto, Complex Script Font: +Headings CS (Times New Roman), 10 pt
Formatted: Font color: Auto

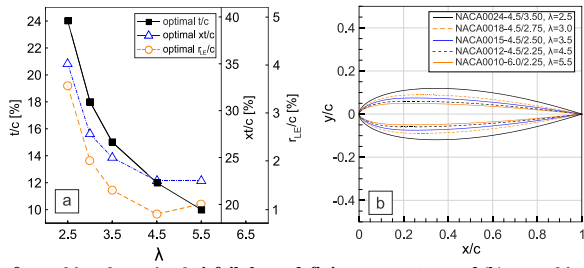
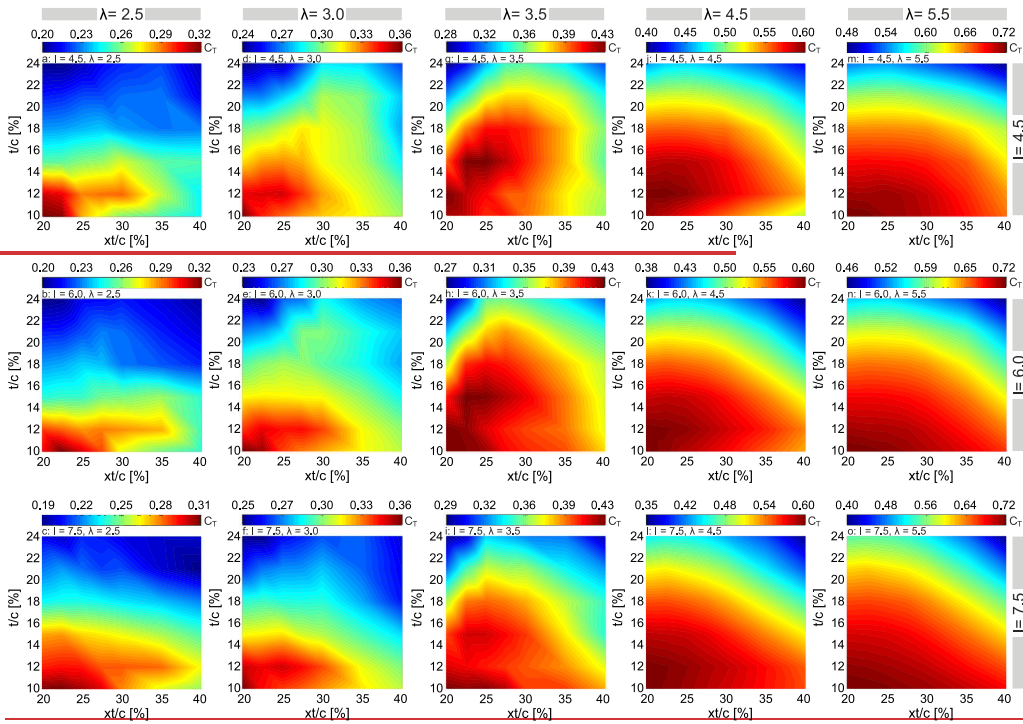


Figure 17. (a): variations of morphing the optimal airfoil shape-defining parameters and (b): morphing optimal airfoil shapes at different λ .

402
403
404



405

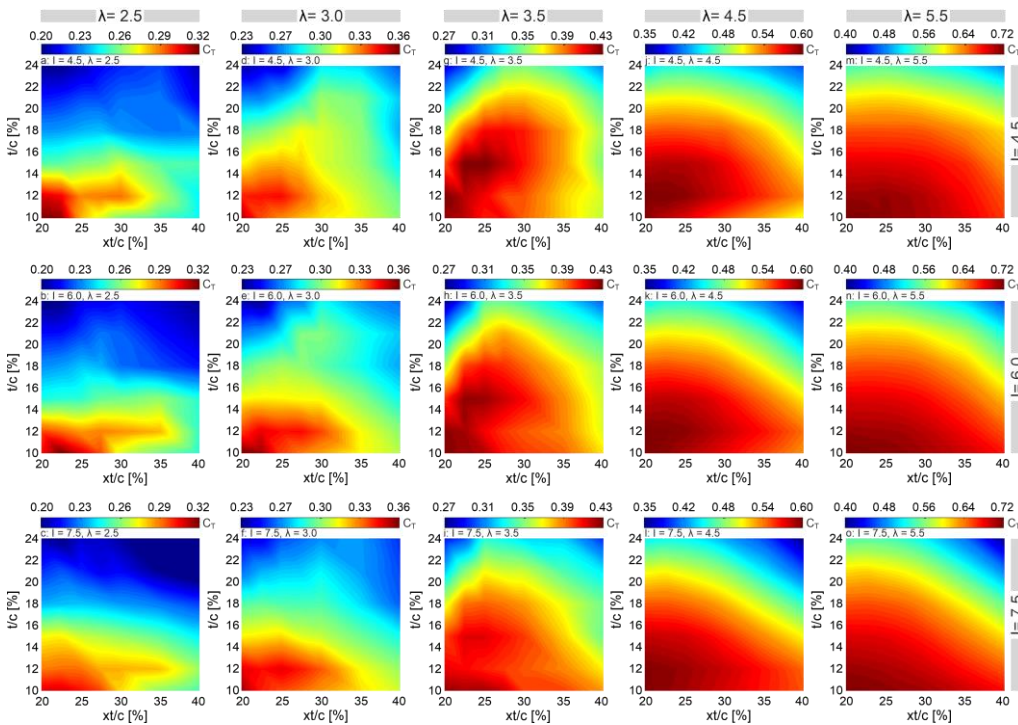


Figure 18: Turbine C_T in $t/c - xt/c$ space. Each contour plot is based on 42 simulations. Colormaps are in different range.

4.2 Towards a morphing blade

This section provides an overview of the turbine power gain due to different morphed-airfoil ing-scenarios, namely a fixed optimal airfoil for each λ (scenario 1), as already discussed in Sect. 1; and an optimal airfoil for each $d\theta$ (scenario 2), as discussed in the following Section. Figure 196 shows the variation of t/c and xt/c versus azimuth for scenario 2. Figure 17–20 shows the corresponding $C_{m,max}$ for each scenario in $\lambda - \theta$ space. Note that scenario 2 is divided into three cases, namely cases A, B and C. In cases A and B, the t_{opt}/c and xt_{opt}/c of the already identified optimal shapes for each λ are kept fixed and distributions of xt/c and t/c versus θ , corresponding to $C_{m,max}$, are extracted, respectively. In case C, the combination of t_{opt}/c and xt_{opt}/c , corresponding to $C_{m,max}$ at each $d\theta$ is selected and kept fixed, and distributions of xt_{opt}/c (i.e., case C1) and t_{opt}/c (i.e., case C2) versus azimuth are extracted, respectively. Note that $I_{opt} = 4.5$ remains invariant for $\lambda \leq 4.5$ and changes to $I_{opt} = 6.0$ only at $\lambda = 5.5$. For the sake of clarity and analysis, $I_{opt} = 4.5$ is assumed to be constant throughout the studied range of λ , introducing the NACA0012-4.5/2.50 as the optimal airfoil at $\lambda = 5.5$. The absolute-relative difference between the $C_{p,max}$ values for optimal airfoils with $I = 4.5$ and 6.0 at $\lambda = 5.5$ is -0.0013005.

Formatted: Adjust space between Latin and Asian text, Adjust space between Asian text and numbers

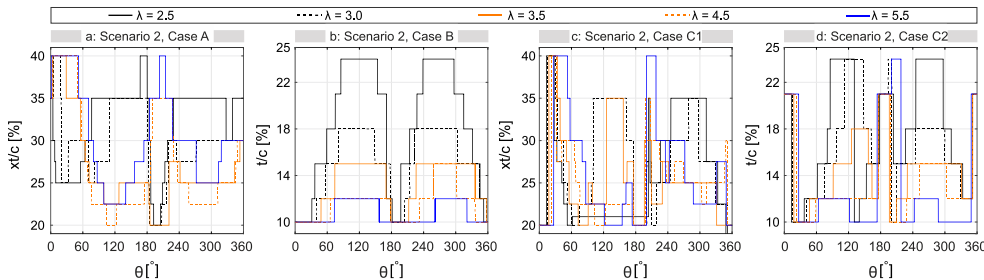


Figure 19: Morphing Changing (a) xt/c and (b) t/c versus azimuth for fixed t_{opt}/c and xt_{opt}/c corresponding to each λ ; morphing changing (c) xt_{opt}/c and (d) t_{opt}/c vs azimuth for fixed t_{opt}/c and xt_{opt}/c corresponding to each $d\theta$.

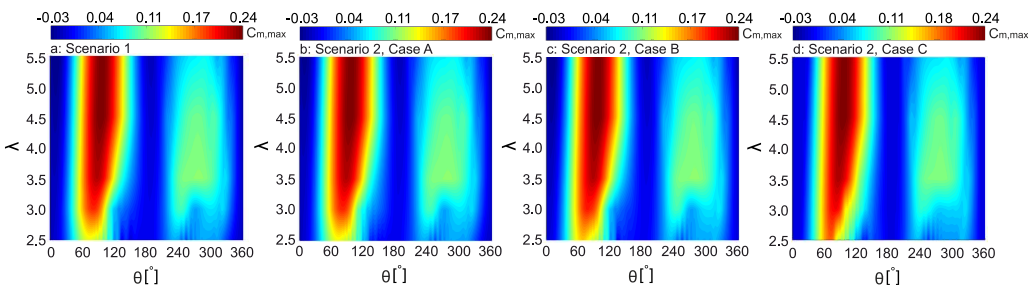


Figure 20: Turbine C_m in $\lambda - \theta$ space for different morphing scenarios.

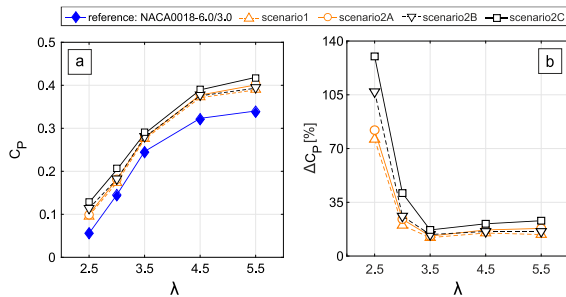


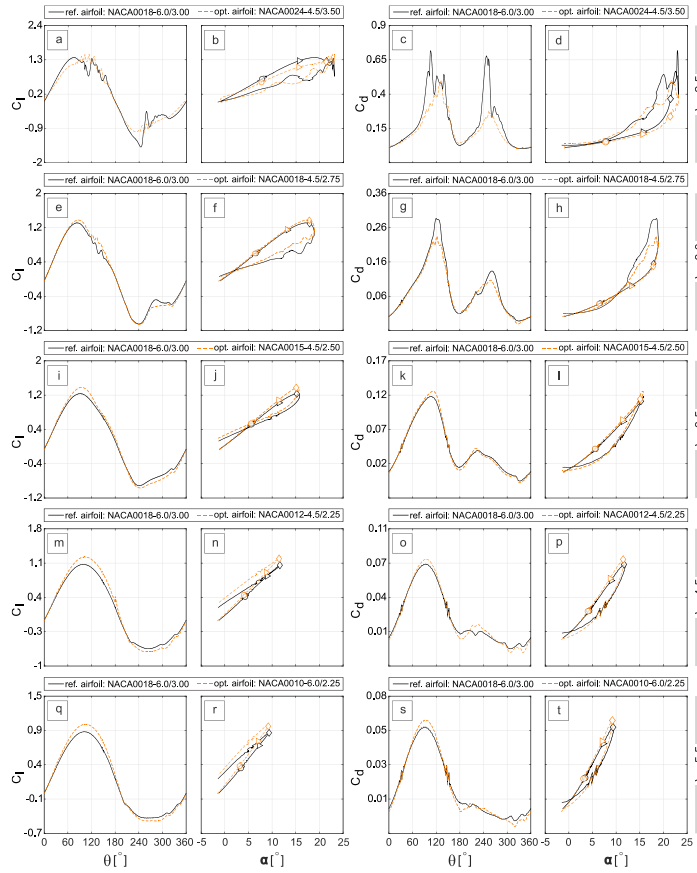
Figure 21: Variations of (a): turbine C_p and (b): power gain due to different scenarios for a morphing blade at different λ .

Figures 196a and 2017b show the results for scenario 2, case A. Note that the results are based on individual simulations for the studied airfoil shapes, and correspond to the xt/c with the highest value of C_m at each $d\theta$. It can be observed that xt/c shows almost the same level of sensitivity to θ for different λ (see Fig. 185 a). Fig. 2017b shows the overall view of the $C_{m,max}$ as the blade section-airfoil rotates-is morphed for different azimuthal position at each λ , and morphs at different λ . Obviously, the maximum torque is obtained around $\theta = 90^\circ$ for different λ . The higher torque generated in the upwind quartile is due to the unperturbed upstream wind profile, while the less pronounced $C_{m,max}$ in the downwind quartile is due to the lower wind velocity and blade-wake interaction.

For scenario 2, case B, the observed trend for $t_{opt}/c - \theta$ is quite similar at-for different λ , except for a noticeable difference; that is, the higher λ is, the less sensitive the variation of t_{opt}/c to θ is. By increasing λ , and thus, decreasing the xt_{opt}/c , thinner airfoils outperform the thicker ones (see Figs. 19b). The turbine $C_{m,max}$ in $\lambda - \theta$ space shows negligible changes compared to that of scenario 2A (see Figs. 20c)(see Figs. 16b and 17b). The observations for scenario 2C1 and 2C2 are almost similar to those of cases A and

Formatted: Font: 9 pt, Font color: Auto, Complex Script
Font: 9 pt

439 B, respectively. However, there are some narrow ranges of θ at the beginning, middle, and end of the turbine rotation disk, where
 440 noticeable differences exist. The resulting $C_{m,max}$ in $\lambda - \theta$ space differs slightly from the other scenarios (see Fig. 2047d).
 441 Figure 2148 shows the turbine C_p and the power gain due to the morphed airfoils and the reference case for the studied range of λ .
 442 The highest average improvement in the turbine C_p is due to scenario 2C (i.e., fixed t_{top}/c and xt_{top}/c , corresponding to the $C_{m,max}$ at
 443 each $d\theta$), different scenarios for a morphing blade versus the reference case at different λ . By increasing λ from 2.5 to 3.5, the power
 444 gain significantly decreases. Nevertheless, for $\lambda \geq 4.5$ it marginally increases. The more pronounced ΔC_p at low λ is mainly because
 445 of alleviating the dynamic stall characteristics due to the morphed airfoil, is due to alleviating the dynamic stall by using a morphing
 446 blade. The averaged improvement in C_p due to scenarios 1, 2A, 2B, and 2C ($\overline{\Delta C_p}$) over the studied range of λ is 0.04, 0.045, 0.047,
 447 and 0.06, respectively.



448
 449 **Figure 22:** C_l and C_d versus θ and α for the reference and morphing optimal airfoils at different λ (\circ : $\theta = 60^\circ$; \triangleright : $\theta = 120^\circ$; \diamond : $\theta = 180^\circ$).

450 **4.3 Aerodynamic analysis of the morphed airfoils**

Formatted: Font: 6 pt, Complex Script Font: 6 pt
Formatted: Font: 7 pt, Complex Script Font: 7 pt
Formatted: Font color: Auto

Figure 2219 gives a comparison of the turbine aerodynamic loads (namely, C_l and C_d) versus θ and α for the reference and **morphingmodified** airfoils. The results correspond to scenario 1, where an optimal airfoil is identified for each λ . In general, the **morphingoptimal** airfoils have higher $C_{l,max}$ compared to that of the reference case. For $\lambda = 2.5$, the **morphingoptimal** airfoil shows an obvious reduction in drag jump both in upwind and downwind quartiles and reduced post-stall fluctuation. These are the reflections of the significantly-alleviated dynamic stall. Table 5 gives the $C_{l,max}$ and $C_{d,max}$ values for the reference and **morphingoptimal** airfoils at different λ . It can be seen that for $\lambda = 3.0$ and 3.5 , where the turbine goes into a lighter-dynamic stall regime, the **morphingoptimal** airfoil shows higher $C_{l,max}$ with less severe post-stall fluctuation and lower $C_{d,max}$ with less substantial drag jump. For $\lambda \geq 4.5$ (i.e., non-dynamic stall regime), although the **morphingmodified** airfoils show higher values for both the $C_{l,max}$ and $C_{d,max}$, the increase in $C_{l,max}$ is more dominant than that of the $C_{d,max}$ (see also Table 5). Figure 230 shows the turbine C_m for the reference and **optimal morphing**-airfoils at each λ . Other than a reduction for $0^\circ \leq \theta \leq 80^\circ$ at $\lambda = 2.5$, the turbine C_m is found to improve moderately due to the **optimal morphing**-airfoils at the studied range of λ , indicating higher turbine C_p .

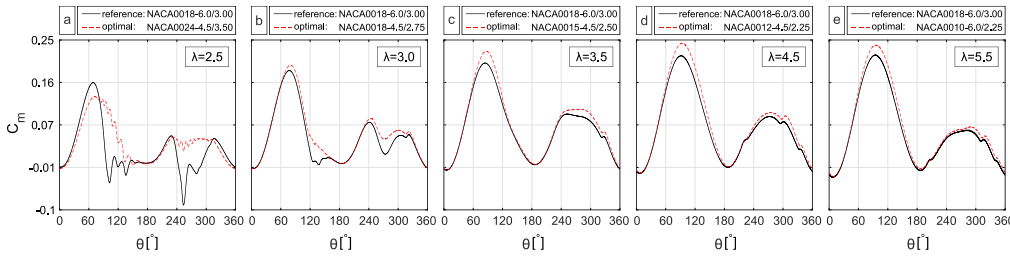


Figure 23: Turbine C_m for the reference and **morphing optimal blades-airfoils** at different λ (scenario 1).

Table 5: Estimated $C_{l,max}$ and $C_{d,max}$ for the reference and optimal airfoils at different λ (scenario 1).

λ	2.5		3.0		3.5		4.5		5.5	
load coefficient	$C_{l,max}$	$C_{d,max}$	$C_{l,max}$	$C_{d,max}$	$C_{l,max}$	$C_{d,max}$	$C_{l,max}$	$C_{d,max}$	$C_{l,max}$	$C_{d,max}$
reference	1.37	0.716	1.31	0.29	1.23	0.118	1.07	0.076	0.93	0.064
morphingmodified	1.47	0.503	1.38	0.24	1.38	0.126	1.23	0.082	1.05	0.059
Difference [%]	+7	-29.8	+5	-17	+12	+6.7	+15	+8	+13	+8.5

5. Discussion

The present work includes a wide range of λ , where the turbine goes into different operational regimes of light-, deep-, and non-dynamic stall regimes. The aim of the analysis is to highlight the power gain of VAWTs due to **different morphed-airfoil scenarios** different scenarios of a morphing blade.

The symmetric modified NACA 4 digit airfoil series is chosen as a basis for the morphing airfoils. The airfoils are generated by setting the three main defining parameters, i.e., t/c , x/c and r_{LE} . It is suggested to continue this work for the rest of important geometrical parameters, such as camber and its position along the chord, which describe the airfoil asymmetry and have the potential to morph.

The results prove the usefulness of the morphing technique to improve the power performance of VAWTs as the main objective of this work. Also, the structural strength of the blade could be another important objective that must be considered while designing morphing blades for VAWTs. It is found that this objective is also satisfied, and the blade structural limitations are met. This is due to the fact that the **morphing** airfoil changes from a thin airfoil-one for the highest λ , corresponding to low wind speeds and aerodynamic loads, to a more robust thick airfoil for the lowest λ , where the lack of strength and stiffness can cause blade failure,

Formatted: Font: Italic, Font color: Auto, Complex Script
Font: Italic

Formatted: Font color: Auto

Formatted: Font: Italic, Font color: Auto, Complex Script
Font: Italic

Formatted: Font color: Auto

Formatted: Font: Italic, Font color: Auto, Complex Script
Font: Italic

Formatted: Font: Italic, Font color: Auto, Complex Script
Font: Italic

Formatted: Font color: Auto

Formatted: Font: Italic, Font color: Auto, Complex Script
Font: Italic

and thus, the blade needs to withstand the aerodynamic loads and to avoid the resultant deflections. However, the maximum and minimum morphing ranges for the airfoil shape-defining parameters might be limited due to manufacturing process. Another technical challenge of utilizing morphing blade for VAWTs is the fatigue failure of the blade due to continuous shape changing. Therefore, an analysis of stresses and fatigue is of high importance to determine the effects of morphing technique on the lifetime of the smart rotor. However, in addition, technical considerations related to the complexity of the electromechanical actuators for the morphing blade must be taken into account. The required actuators need to be chosen such that they can meet the displacement requirements at the given response times and rotational speeds in Table 6, which might be unfeasible for very small values of $d\theta$. However, extracting the optimal airfoils corresponding to higher values of $d\theta$ (e.g., $d\theta = 30^\circ, 45^\circ$, and 90°) could result in much higher values of response time and thus, makes it technically possible to adapt the shape changes with azimuthal position at the corresponding response times and rotational speeds. In addition, it is of particular importance to consider the cost factor and feasibility of such a system and also to estimate the contribution of morphing blade in annual energy production of the wind turbine for an annual average wind speed, i.e., the difference between the power required to drive the actuators and the resulting turbine power gain.

Table 6: Actuator response time for the blade to morph at $\lambda = 2.5, 3.0, 3.5, 4.5$ and 5.5 .

λ	Ω (rad/sec)	Ω (deg/sec)	RPS	Response time (ms)
2.5	46.5	2664	7.4	0.37
3.0	55.8	3197	8.8	0.31
3.5	65.1	3730	10.4	0.27
4.5	83.7	4795	13.3	0.21
5.5	93	5328	14.8	0.19

Note: RPS (revolution per second); ms (millisecond)

6. Limitations

6.1 Geometrical parameters

The symmetric modified NACA 4-digit airfoil series is chosen as a basis for the studied airfoils. The airfoils are generated by changing the three main defining parameters, i.e., t/c , x/c and r_{TE} . However, it is suggested to continue this work for the rest of the parameters, such as camber and its position along the chord, which describe the airfoil asymmetry and have the potential to morph. The number of blades (n) and solidity (σ) are another two important parameters that would also impact the turbine performance. Some attempts have been made to study the impact of these parameters on turbine performance (Rezaeiha et al., 2018a; Subramanian et al., 2017). For example, it was shown that for different λ , at a given Re_c the variations of α are almost independent of n . In addition, increasing solidity decreases the variations of α at different λ (Rezaeiha et al., 2018a). Therefore, based on the results presented in sect. 4.2, it is expected that for 2-, 3- and 4-bladed VAWTs, the airfoil shape-defining parameters show the same level of sensitivity to θ ; and for higher σ , the airfoil parameters show less pronounced sensitivity to θ . However, due to high computational costs, the focus of this work as the first step in designing smart rotors, is confined to investigating the impact of airfoil parameters for a single-blade turbine with a fixed solidity. In addition, due to the large number of simulations in this work, the location of the blade-spoke connection is considered fixed at $c/2$. Nonetheless, for real application scenarios, dedicated investigations are required to study the sensitivity of the optimal regions for the airfoil shape-defining parameters to the number of blades, solidity, and the blade/spoke connection point.

5.16.2 Unsteady aerodynamics

Formatted: Font color: Auto

Formatted: Font: 10 pt, Complex Script Font: 10 pt

Formatted: Font: (Default) +Headings CS (Times New Roman), 10 pt, Font color: Auto, Complex Script Font: +Headings CS (Times New Roman), 10 pt, Pattern: Clear

Formatted

Formatted

Formatted: Font color: Auto

Formatted

Formatted

Formatted

Formatted

Formatted

Formatted: Font color: Auto

Formatted

Formatted

Formatted

Formatted

Formatted

Formatted

Formatted

Formatted

Formatted

Formatted

Formatted

Formatted

Formatted

Formatted

Formatted

Formatted

Formatted

Formatted

Formatted

Formatted

Formatted

Formatted: Font color: Auto

Formatted: Font color: Auto

Formatted: Font: 10 pt, Complex Script Font: 10 pt

Formatted

Formatted

Formatted: Font color: Auto

509 The present study is performed based on a quasi-static assumption where the optimal airfoils at each $d\theta$ are selected from individual
510 simulations for the studied airfoil shapes. Therefore, the effect of the varying unsteady change in bound circulation due to the
511 morphing blade has been considered negligible, and hence no shed vorticity is assumed as a result of the bound circulation temporal
512 gradient. The presented results, as the first step on the way to the smart rotor design, can be utilized as primary tools for quasi-
513 dynamic simulations, where a more focused analysis on a morphing blade scenario would inevitably have to include the mentioned
514 effect; but in view of the major aims put forward in this work, this scenario is left for future studies.

Formatted: Font: 10 pt, Font color: Auto, Complex Script Font: 10 pt

515 5.26.3 Operational parameters

516 The present study is focused on a fixed Reynolds number (Re), turbulence intensity (TI) and reduced frequency (K). In an extensive
517 numerical study by (Rezaeiha et al., 2018b), it was shown that the variations of α and normalized V_{rot} are almost independent of
518 Re and TI . Nevertheless, dedicated studies are mandatory to draw definitive conclusions concerning the impact of these parameters
519 on the optimal region of airfoil geometrical parameters.

Formatted: Font: 9 pt, Complex Script Font: +Headings CS (Times New Roman), 9 pt

520 5.36.4 Modeling approach

521 In the present study 2D URANS simulations are conducted, representing the midplane of a turbine with a high aspect ratio and
522 negligible 3D tip effects. The 2D simulations are chosen based on our earlier study, where the results from 2D and 2.5D simulations
523 for a VAWT with a given λ and σ showed negligible differences (<1%) in power and thrust coefficients (C_p and C_T) (Rezaeiha et
524 al., 2017a). However, compared with the more computationally expensive approaches such as scale-resolving simulations (SAS)
525 and hybrid RANS/LES, the URANS approach fails to provide accurate prediction of the turbine power performance under the
526 influence of the dynamic stall characteristics at low λ (i.e., formation, growth, bursting/shedding of the LSB, dynamic stall vortex
527 (DSV), and trailing edge vortex (TEV)) (Rezaeiha et al., 2019a).

Formatted: Normal, Justified, Indent: Before: 0", Space After: 0 pt

Formatted: Font: Not Bold, Italic, Font color: Auto, Complex Script Font: Not Bold, Italic

528 6.7. Conclusions

529 Incompressible URANS simulations, previously validated with experiments, are used to study the impact of different morphed-
530 airfoil scenarios scenarios of a morphing blade on the power and thrust performance of a VAWT. Three main airfoil shape-defining
531 parameter, namely t/c , xt/c and I , are chosen and morphed-modified as functions of λ and θ to determine the optimal airfoils in
532 terms of C_p in a wide range of λ .

Formatted: Normal, Justified, Indent: Before: 0", Space After: 0 pt

Formatted: Font: Not Bold, Italic, Font color: Auto, Complex Script Font: Not Bold, Italic

533 The main conclusions are as follows:

Formatted: Font color: Auto

- 534 - For each λ , there exists an optimal -morphing airfoil shape, corresponding to the turbine $C_{p,max}$. At the lowest $\lambda = 2.5$, the
535 modifiedorphing airfoil is defined with $t/c = 24\%$, $xt/c = 35\%$ and $I = 4.5$ (i.e., the NACA0024-4.5/3.5). In comparison to
536 the baseline airfoil (i.e., the NACA0018-6.0/3.0), this airfoil has a smaller leading-edge radius; and a higher maximum
537 thickness, which is found to shift downstream of the default point by 5%.
- 538 - By increasing λ , the combination of t_{opt}/c and xt_{opt}/c morphs-changes to lower values; however, it shows less dependency on
539 r_{LE} . For $\lambda = 3.0, 3.5, 4.5$, and 5.5 , the optimal airfoils are the morphs to-NACA0018-4.5/2.75, NACA0015-4.5/2.50,
540 NACA0012-4.5/2.25 and NACA0010-6.0/2.25, respectively.
- 541 - Regarding the modifiedrphing airfoil as a function of θ , the highest average improvement in the turbine C_p is due to scenario
542 2C, where the combination of t_{opt}/c and xt_{opt}/c , corresponding to the turbine $C_{m,max}$ at each $d\theta$, is selected and kept fixed.
- 543 - The improvement in C_p due to morphing-modifying blade becomes more pronounced for low values of λ , where the adverse
544 effects of dynamic stall, i.e., jump in aerodynamic loads and post-stall loads fluctuation, are mitigated by morpheding airfoils.

Formatted: Font: Italic, Complex Script Font: Italic

Formatted: Font: Italic, Complex Script Font: Italic

The presented work not only highlights the strong relevance of the gain in turbine C_P to different scenarios for morphing blade airfoils scenario but also emphasizes the combined morphing-changing of the airfoil shape-defining parameters. That is, single-parameter morphing-modification will not result in the highest power improvement of VAWTs. Other important considerations, such as morphing-changing the rest of the e-geometrical parameters (e.g., camber and its chordwise position, blade/spoke connection point, number of blades, and solidity), are yet to be determined. Therefore, the present study could be a significant stride towards future studies on designing advanced morphing blades for smart VAWTs.

Formatted: Font color: Auto

Acknowledgement

The first author acknowledges the support from his home university for the use of supercomputing facilities. The second author is currently a postdoctoral fellow of the Research Foundation – Flanders (FWO) and is grateful for the financial support (project FWO 12ZP520N).

References

- Ajaj, R. M., Parancheerivilakkathil, M. S., Amoozgar, M., Friswell, M. I., and Cantwell, W. J.: Recent developments in the aeroelasticity of morphing aircraft, Prog. Aerosp. Sci., 120, 100682, <https://doi.org/10.1016/j.paerosci.2020.100682>, 2021.
- Balduzzi, F., Bianchini, A., Ferrara, G., and Ferrari, L.: Dimensionless numbers for the assessment of mesh and timestep requirements in CFD simulations of Darrieus wind turbines, Energy, 97, 246-261, <https://doi.org/10.1016/j.energy.2015.12.111>, 2016a.
- Balduzzi, F., Bianchini, A., Maleci, R., Ferrara, G., and Ferrari, L.: Critical issues in the CFD simulation of Darrieus wind turbines, Renew. Energ., 85, 419-435, <https://doi.org/10.1016/j.renene.2015.06.048>, 2016b.
- Barbarino, S., Bilgen, O., Ajaj, R. M., Friswell, M. I., and Inman, D. J.: A Review of Morphing Aircraft, J Intell Mater Syst Struct, 22, 823-877, <https://doi.org/10.1177/1045389X11414084>, 2011.
- Bedon, G., De Betta, S., and Benini, E.: Performance-optimized airfoil for Darrieus wind turbines, Renew. Energ., 94, 328-340, <https://doi.org/10.1016/j.renene.2016.03.071>, 2016.
- Beyene, A. and Peffley, J.: A morphing blade for wave and wind energy conversion, OCEANS 2007 - Europe, Aberdeen, UK, 18-21 June 2007, 1-6, <https://doi.org/10.1109/OCEANSE.2007.4302482>, 2007.
- Bianchini, A., Ferrara, G., and Ferrari, L.: Design guidelines for H-Darrieus wind turbines: Optimization of the annual energy yield, Energy Convers. Manag., 89, 690-707, <https://doi.org/10.1016/j.enconman.2014.10.038>, 2015.
- Castelli, M. R., Englaro, A., and Benini, E.: The Darrieus wind turbine: proposal for a new performance prediction model based on CFD, J. Energy, 36, 4919-4934, <https://doi.org/10.1016/j.energy.2011.05.036>, 2011.
- Coiro, D., Nicolosi, F., De Marco, A., Melone, S., and Montella, F.: Flow Curvature Effect on Dynamic Behaviour of a Novel Vertical Axis Tidal Current Turbine: Numerical and Experimental Analysis, ASME 2005 24th International Conference on Offshore Mechanics and Arctic Engineering, Halkidiki, Greece, 12-17 June 2005, 601-609, <https://doi.org/10.1115/omae2005-67193>, 2005.
- Daynes, S. and Weaver, P. M.: A morphing trailing edge device for a wind turbine, J Intell Mater Syst Struct, 23, 691-701, <https://doi.org/10.1177/1045389X12438622>, 2012.
- Debiasi, M., Khoo, H. H., Bouremel, Y., Luo, S. c., and Zhiwei, E.: Shape change of the upper surface of an airfoil by macro fiber composite actuators, 29th AIAA Applied Aerodynamics Conference, Hawaii, 27-30 June 2011, <https://doi.org/10.2514/6.2011-3809>, 2011.
- E.Amet, Maitre, T., Pellone, C., and Achard, j.-l.: 2D Numerical simulations of blade-vortex interaction in a Darrieus turbine, J. Fluids Eng., 131, 1-15, <https://doi.org/10.1115/1.4000258>, 2009.
- Ferreira, C. S., Van Kuik, G., Van Bussel, G., and Scarano, F.: Visualization by PIV of dynamic stall on a vertical axis wind turbine, Exp Fluids, 46, 97-108, <https://doi.org/10.1007/s00348-008-0543-z>, 2009.
- Frolov, V. A.: Laminar separation point of flow on surface of symmetrical airfoil, Proceedings of the 18th International Conference on the Methods of Aerophysical Research, Perm, Russia, 27 June – 3 July 2016, 030053, <https://doi.org/10.1063/1.4963995>, 2016.
- Hand, B., Kelly, G., and Cashman, A.: Numerical simulation of a vertical axis wind turbine airfoil experiencing dynamic stall at high Reynolds numbers, Comput Fluids, 149, 12-30, <https://doi.org/10.1016/j.compfluid.2017.02.021>, 2017.
- Healy, J.: The influence of blade thickness on the output of vertical axis wind turbines, J. Wind Energy, 2, 1-9, 1978.
- Ismail, M. F. and Vijayaraghavan, K.: The effects of aerofoil profile modification on a vertical axis wind turbine performance, Energy, 80, 20-31, <https://doi.org/10.1016/j.energy.2014.11.034>, 2015.
- Jain, S. and Saha, U. K.: On the influence of blade thickness-to-chord ratio on dynamic stall phenomenon in H-type Darrieus wind rotors, Energy Convers. Manag., 218, 113024, <https://doi.org/10.1016/j.enconman.2020.113024>, 2020.
- Lachenal, X., Daynes, S., and Weaver, P. M.: A zero torsional stiffness twist morphing blade as a wind turbine load alleviation device, Smart Mater. Struct., 22, 065016, <https://doi.org/10.1088/0964-1726/22/6/065016>, 2013.

597 Ma, N., Lei, H., Han, Z., Zhou, D., Bao, Y., Zhang, K., Zhou, L., and Chen, C.: Airfoil optimization to improve power performance
598 of a high-solidity vertical axis wind turbine at a moderate tip speed ratio, *J. Energy*, 150, 236-252,
599 <https://doi.org/10.1016/j.energy.2018.02.115>, 2018.

600 MacPhee, D. W. and Beyene, A.: Experimental and fluid structure interaction analysis of a morphing wind turbine rotor, *J. Energy*,
601 90, 1055-1065, <https://doi.org/10.1016/j.energy.2015.08.016>, 2015.

602 Mazarbhuiya, H. M. S. M., Biswas, A., and Sharma, K. K.: Blade thickness effect on the aerodynamic performance of an
603 asymmetric NACA six series blade vertical axis wind turbine in low wind speed, *Int. J. Green Energy*, 17, 171-179,
604 <https://doi.org/10.1080/15435075.2020.1712214>, 2020.

605 McCroskey, W. J.: The phenomenon of dynamic stall, NASA TM 81264, NASA, Moffett Field CA. ARC, 1981.

606 Melani, P. F., Balduzzi, F., Ferrara, G., and Bianchini, A.: How to extract the angle attack on airfoils in cycloidal motion from a
607 flow field solved with computational fluid dynamics? Development and verification of a robust computational procedure, *Energy*
608 *Convers. Manag.*, 223, 113284, <https://doi.org/10.1016/j.enconman.2020.113284>, 2020.

609 Meseguer, J., Alonso, G., Sanz-Andrés, A., and Pérez-Grande, I.: On the circulation and the position of the forward stagnation
610 point on airfoils, *Int. J. Mech. Eng. Educ.*, 35, 65-75, <https://doi.org/10.7227/IJMEE.35.1.5>, 2007.

611 Migliore, P., Fanucci, J., and Wolfe, W.: Flow Curvature Effects on Darrieus Turbine Blade Aerodynamics, *J. Energy*, 4, 49-55,
612 <https://doi.org/10.2514/3.62459>, 1980.

613 Minetto, R. A. L. and Paraschivoiu, M.: Simulation based analysis of morphing blades applied to a vertical axis wind turbine, *J.*
614 *Energy*, 202, 117705, <https://doi.org/10.1016/j.energy.2020.117705>, 2020.

615 Mir, I., Maqsood, A., Eisa, S. A., Taha, H., and Akhtar, S.: Optimal morphing – augmented dynamic soaring maneuvers for
616 unmanned air vehicle capable of span and sweep morphologies, *Aerosp. Sci. Technol.*, 79, 17-36,
617 <https://doi.org/10.1016/j.ast.2018.05.024>, 2018.

618 Mulleners, K. and Raffel, M.: The onset of dynamic stall revisited, *Exp Fluids*, 52, 779-793, <https://doi.org/10.1007/s00348-011-1118-y>, 2012.

619

620 Nguyen, C.-C. and Tran, P.-T.: A numerical study of thickness effect of the symmetric NACA 4-digit airfoils on self starting
621 capability of a 1kW H-type vertical axis wind turbine, *J. mech. eng. appl.*, 3, 7-16,
622 <https://doi.org/10.11648/j.ijmea.s.2015030301.12>, 2015.

623 Pechlivanoglou, G., Wagner, J., Nayeri, C., and Paschereit, C.: Active aerodynamic control of wind turbine blades with high
624 deflection flexible flaps, 48th AIAA Aerospace Sciences Meeting Including the New Horizons Forum and Aerospace Exposition,
625 Orlando, Florida, 4-7 January 2010, <https://doi.org/10.2514/6.2010-644>, 2010.

626 Rainbird, J. M., Bianchini, A., Balduzzi, F., Peiró, J., Graham, J. M. R., Ferrara, G., and Ferrari, L.: On the influence of virtual
627 camber effect on airfoil polars for use in simulations of Darrieus wind turbines, *Energy Convers. Manag.*, 106, 373-384,
628 <https://doi.org/10.1016/j.enconman.2015.09.053>, 2015.

629 Rezaeiha, A., Kalkman, I. M., and Blocken, B.: CFD simulation of a vertical axis wind turbine operating at a moderate tip speed
630 ratio: guidelines for minimum domain size and azimuthal increment, *Renew. Energ.*, 107, 373-385,
631 <https://doi.org/10.1016/j.renene.2017.02.006>, 2017a.

632 Rezaeiha, A., Montazeri, H., and Blocken, B.: Towards optimal aerodynamic design of vertical axis wind turbines: Impact of
633 solidity and number of blades, *J. Energy*, 165, 1129-1148, <https://doi.org/10.1016/j.energy.2018.09.192>, 2018a.

634 Rezaeiha, A., Montazeri, H., and Blocken, B.: Characterization of aerodynamic performance of vertical axis wind turbines: impact
635 of operational parameters, *Energy Convers. Manag.*, 169, 45-77, <https://doi.org/10.1016/j.enconman.2018.05.042>, 2018b.

636 Rezaeiha, A., Montazeri, H., and Blocken, B.: Towards accurate CFD simulations of vertical axis wind turbines at different tip
637 speed ratios and solidities: Guidelines for azimuthal increment, domain size and convergence, *Energy Convers. Manag.*, 156, 301-
638 316, <https://doi.org/10.1016/j.enconman.2017.11.026>, 2018c.

639 Rezaeiha, A., Montazeri, H., and Blocken, B.: CFD analysis of dynamic stall on vertical axis wind turbines using Scale-Adaptive
640 simulation (SAS): Comparison against URANS and hybrid RANS/LES, *Energy Convers. Manag.*, 196, 1282-1298,
641 <https://doi.org/10.1016/j.enconman.2019.06.081>, 2019a.

642 Rezaeiha, A., Montazeri, H., and Blocken, B.: On the accuracy of turbulence models for CFD simulations of vertical axis wind
643 turbines, *J. Energy*, 180, 838-857, <https://doi.org/10.1016/j.energy.2019.05.053>, 2019b.

644 Rezaeiha, A., Montazeri, H., and Blocken, B.: Active flow control for power enhancement of vertical axis wind turbines: Leading-
645 edge slot suction, *J. Energy*, 189, 116131, <https://doi.org/10.1016/j.energy.2019.116131>, 2019c.

646 Rezaeiha, A., Montazeri, H., and Blocken, B.: Scale-Adaptive Simulation (SAS) of Dynamic Stall on a Wind Turbine, 1, *Progress*
647 *in Hybrid RANS-LES Modelling (HRLM 2018)*, 143, Springer International Publishing, https://doi.org/10.1007/978-3-030-27607-2_26, 2020a.

648

649 Rezaeiha, A., Montazeri, H., and Blocken, B.: A framework for preliminary large-scale urban wind energy potential assessment:
650 Roof-mounted wind turbines, *Energy Convers. Manag.*, 214, 112770, <https://doi.org/10.1016/j.enconman.2020.112770>, 2020b.

651 Rezaeiha, A., Kalkman, I., Montazeri, H., and Blocken, B.: Effect of the shaft on the aerodynamic performance of urban vertical
652 axis wind turbines, *Energy Convers. Manag.*, 149, 616-630, <https://doi.org/10.1016/j.enconman.2017.07.055>, 2017b.

653 Riemenschneider, J., Balzarek, C., van der Wall, B. G., and Majeti, R. K.: Chord Morphing for Helicopter Rotor Blades, *ASME*
654 *2019 Conference on Smart Materials, Adaptive Structures and Intelligent Systems*, Kentucky, 9–11 September 2019,
655 <https://doi.org/10.1115/SMASIS2019-5625>, 2019.

656 Sahebzadeh, S., Rezaeiha, A., and Montazeri, H.: Towards optimal layout design of vertical-axis wind-turbine farms: Double rotor
657 arrangements, *Energy Convers. Manag.*, 226, 113527, <https://doi.org/10.1016/j.enconman.2020.113527>, 2020.
658 Sal, F.: Effects of the actively morphing root chord and taper on helicopter energy, *Aircr. Eng. Aerosp. Technol.*, 92, 264-270,
659 <https://doi.org/10.1108/AEAT-08-2019-0165>, 2020.
660 Sharma, A. and Visbal, M.: Numerical investigation of the effect of airfoil thickness on onset of dynamic stall, *J. Fluid Mech.*,
661 870, 870-900, <https://doi.org/10.1017/jfm.2019.235>, 2019.
662 Siddall, R., Ortega Ancel, A., and Kovač, M.: Wind and water tunnel testing of a morphing aquatic micro air vehicle, *Interface*
663 *Focus*, 7, 20160085, <https://doi.org/10.1098/rsfs.2016.0085>, 2017.
664 Song, C., Wu, G., Zhu, W., and Zhang, X.: Study on aerodynamic characteristics of Darrieus vertical axis wind turbines with
665 different airfoil maximum thicknesses through computational fluid dynamics, *Arab. J. Sci. Eng.*, 45, 689-698,
666 <https://doi.org/10.1007/s13369-019-04127-8>, 2020.
667 Subramanian, A., Yogesh, S. A., Sivanandan, H., Giri, A., Vasudevan, M., Mugundhan, V., and Velamati, R. K.: Effect of airfoil
668 and solidity on performance of small scale vertical axis wind turbine using three dimensional CFD model, *J. Energy*, 133, 179-
669 190, <https://doi.org/10.1016/j.energy.2017.05.118>, 2017.
670 Tan, J. and Paraschivoiu, M.: CFD-based performance analysis of morphing aileron for vertical axis wind turbines, 35th AIAA
671 Applied Aerodynamics Conference, Denver, Colorado, 5-9 June 2017, <https://doi.org/10.2514/6.2017-4072>, 2017.
672 Tescione, G., Ragni, D., He, C., Ferreira, C., and van Bussel, G. J. W.: Near wake flow analysis of a vertical axis wind turbine by
673 stereoscopic particle image velocimetry, *Renew. Energ.*, 70, 47-61, <https://doi.org/10.1016/j.renene.2014.02.042>, 2014.
674 Thangeswaran, R. S. K., Venkateswaran, S., Kalaiselvan, T., Aravindan, P., and Venugopal, S.: Aerodynamic benefits of flexible
675 morphing airfoil for UAV, 12th EURECA 2019: 12th International Engineering Research Conference, July 3-4 2019, 020002,
676 <https://doi.org/10.1063/1.5120189>, 2019.
677 Tirandaz, M. R. and Rezaeiha, A.: Effect of airfoil shape on power performance of vertical axis wind turbines in dynamic stall:
678 Symmetric Airfoils, *Renew. Energ.*, 173, 422-441, <https://doi.org/10.1016/j.renene.2021.03.142>, 2021.
679 Wang, W., Caro, S., Fouad, B., and Salinas Mejia, O. R.: A simplified morphing blade for horizontal axis wind turbines, *J. Sol.*
680 *Energy Eng.*, 136, 011018-011011-011018-011018, <https://doi.org/10.1115/1.4025970>, 2014.
681 Wlezien, R., Horner, G., McGowan, A., Padula, S., Scott, M., Silcox, R., and Simpson, J.: The Aircraft Morphing Program, 39th
682 AIAA/ASME/ASCE/AHS/ASC Structures, Structural Dynamics, and Materials Conference and Exhibit, Long Beach, CA,
683 <https://doi.org/10.2514/6.1998-1927>, 1998.
684 Wolff, T., Ernst, B., and Seume, J. R.: Aerodynamic behavior of an airfoil with morphing trailing edge for wind turbine
685 applications, *J Phys Conf Ser*, 524, 12-18, <https://doi.org/10.1088/1742-6596/524/1/012018>, 2014.
686 Yan, B., Dai, P., Liu, R., Xing, M., and Liu, S.: Adaptive super-twisting sliding mode control of variable sweep morphing aircraft,
687 *Aerosp Sci Technol*, 92, 198-210, <https://doi.org/10.1016/j.ast.2019.05.063>, 2019.
688 Zhuang, C., Yang, G., Zhu, Y., and Hu, D.: Effect of morphed trailing-edge flap on aerodynamic load control for a wind turbine
689 blade section, *Renew. Energ.*, 148, 964-974, <https://doi.org/10.1016/j.renene.2019.10.082>, 2020.
690